HHS Public Access

Author manuscript

Sci Signal. Author manuscript; available in PMC 2023 March 17.

Published in final edited form as:

Sci Signal. 2023 February 14; 16(772): eabq7842. doi:10.1126/scisignal.abq7842.

Catalytic-site mutations confer multiple states of G protein activation

Natalie Hewitt[1], **Ning Ma**[2], **Nadia Arang**[3,4], **Sarah A. Martin**[1], **Ajit Prakash**[5], **Jeffrey F. DiBerto**[1], **Kevin M. Knight**[1], **Soumadwip Ghosh**[2,6], **Reid H. J. Olsen**[1,7], **Bryan L. Roth**[1], **J. Silvio Gutkind**[3,4,*], **Nagarajan Vaidehi**[2,*], **Sharon L. Campbell**[5,8,*], **Henrik G. Dohlman**[1,8,*]

[1]Department of Pharmacology, University of North Carolina at Chapel Hill, Chapel Hill, NC 27599, USA.

[2]Department of Computational and Quantitative Medicine, Beckman Research Institute of the City of Hope, Duarte, CA 91010, USA.

[3]Department of Pharmacology, University of California San Diego, San Diego, CA, 92093, USA.

[4]Moores Cancer Center, University of California San Diego, La Jolla, CA 92093, USA.

[5]Department of Biochemistry and Biophysics, University of North Carolina at Chapel Hill, Chapel Hill, NC 27599, USA.

[6]Current address: Illumina Inc, 5200 Illumina Way, San Diego, CA 92037, USA.

[7]Current address: GPCR Pharmacology, Discovery Biology, Exscientia Ai, Oxford, UK OX4 4GE.

[8]Lineberger Comprehensive Cancer Center, University of North Carolina at Chapel Hill, Chapel Hill, NC 27599, USA.

Abstract

Heterotrimeric guanine nucleotide-binding proteins (G proteins) that function as molecular switches for cellular growth and metabolism are activated by GTP and inactivated by GTP hydrolysis. A conserved glutamine residue critical for GTP hydrolysis in the G protein α-subunit is often mutated in $G\alpha_q$ or $G\alpha_{11}$, to either leucine or proline, in uveal melanoma. In contrast, other glutamine mutations or mutations in other Gα subtypes are rare. To uncover the mechanism of the genetic selection and the functional role of this glutamine, we analyzed all possible substitutions of this residue in multiple Gα isoforms. Through cell-based measurements of activity, we showed that some mutants were further activated and inactivated by G protein-coupled

*Corresponding author. sgutkind@health.ucsd.edu (J.S.G.); NVaidehi@coh.org (N.V.); campbesl@med.unc.edu (S.L.C.); hdohlman@med.unc.edu (H.G.D.).

Author contributions: N.H., J.S.G., N.V., S.L.C., and H.G.D. designed the project; N.H., N.M., N.A., S.A.M., A.P., J.F.D., K.M.K., S.G., and R.H.J.O. performed experiments and analyzed data; N.H., N.V., S.L.C., and H.G.D wrote the manuscript; N.H., N.M., N.A., S.A.M., A.P., J.F.D., K.M.K., S.G., and R.H.J.O. prepared figures; J.S.G., N.V., S.L.C., and H.G.D. secured funding and supervised the project.

SUPPLEMENTARY MATERIALS

Figs. S1 to S6.

Tables S1 to S4.

Movies showing the motion of PC1 and PC2

Competing interests: J.S.G. reports consulting fees from Domain Pharmaceuticals, Pangea Therapeutics, and io9, and is founder of Kadima Pharmaceuticals. All other authors declare that they have no competing interests.

receptors (GPCRs). Through biochemical, molecular dynamics, and nuclear magnetic resonance (NMR)-based structural studies, we showed that the Gα mutants were functionally distinct and conformationally diverse, despite their shared inability to hydrolyze GTP. Thus, the catalytic glutamine residue contributes to functions beyond GTP hydrolysis, and these functions include subtype-specific allosteric modulation of receptor-mediated subunit dissociation. We conclude that G proteins do not function as simple on-off switches. Rather, signaling emerges from an ensemble of active states, a subset of which are favored in disease and may be uniquely responsive to receptor-directed ligands.

INTRODUCTION

Heterotrimeric guanine nucleotide-binding protein (G protein)-coupled receptors (GPCRs) recognize a broad array of drugs, hormones, neurotransmitters, and sensory signals, such as light, taste, and odors (1). Upon receptor activation, the G protein undergoes molecular rearrangements leading to the activation of effector proteins such as adenylyl cyclases, phosphodiesterases, ion channels, and phospholipase C, among others. Together, these events give rise to second messengers, which are involved in regulating a host of cellular growth and metabolic processes (2–5).

Heterotrimeric G proteins consist of three subunits: an α subunit and an obligate βγ heterodimer. The subunits are inactive when the Gα subunit is bound to GDP and Gβγ. Exchange of GDP for GTP leads to conformational changes in Gα, dissociation of Gβγ from the Gα subunit, and subsequent interaction of these subunits with their respective effectors. The intrinsic cycling of guanine nucleotides is controlled by GPCRs, which accelerate GTP binding, and by regulators of G protein signaling (RGS) proteins, which accelerate GTP hydrolysis (6, 7). Thus, the timing of cellular signaling is a complex interplay between intrinsic exchange and hydrolysis rates, which vary by subtype, and the influence of regulatory proteins.

Nucleotide-dependent conformational changes occur primarily within three flexible regions named Switch I, Switch II, and Switch III (8). In particular, Switch II contains a conserved catalytic glutamine residue, Gln^{204} in $G\alpha_{i1}$, that is critical for GTPase activity (9). The glutamine coordinates the nucleophilic water molecule that is responsible for hydrolysis and release of the γ-phosphate from GTP (10). Consistent with the important role of this glutamine residue in catalysis, Gα mutants lacking the glutamine are unable to hydrolyze GTP, even in the presence of a GTPase-activating protein (11), and are considered to be the oncogenic drivers in several cancers (12). However, the Catalogue of Somatic Mutations in Cancer (COSMIC) database reports an unequal distribution of naturally occurring oncogenic substitutions in Gα. For example, the glutamine-to-leucine (QL) and glutamine-to-proline (QP) mutations occur most frequently in $G\alpha_q$ and $G\alpha_{11}$, whereas other substitutions at this site, or in other Gα subtypes, are less frequent (Fig. 1, A and B) (13). Additionally, COSMIC reports a predominance of these mutations in uveal melanoma (Fig. 1C). A nonrandom pattern of mutagenesis has likewise been observed for oncogenic forms of RAS (14). Whereas most KRAS mutations occur at Gly^{12}, most NRAS mutations occur at Gln^{61}. Whereas $KRAS^{G12D}$ mutations are most common in pancreatic cancer, $KRAS^{G12C}$

is most prevalent in non-small-cell lung cancer. Thus, among both the large and small G protein families, there appears to be a strong genetic selection for certain substitutions, in selected isoforms, and in just a few distinct cell types. We speculate that the most common substitutions are compatible with rapid cell growth, whereas others evoke oncogene-induced differentiation, senescence, cell cycle arrest, cell death, or apoptosis.

The mechanism(s) responsible for mutational bias in oncogenic Gα is unclear. It has been suggested that the prevalence of glutamine-to-leucine or glutamine-to-proline mutations is due to cytosine-to-thymidine transversions that result from exposure to ultraviolet light, which is important for the development of certain cancers. However, the catalytic glutamine in $G\alpha_q$ does not have a base-pair composition that would exhibit this transversion (13). Based on these observations, we instead hypothesized that the mutational preferences reflect differences in the signaling properties of the various Gα subtypes and mutants, including their interactions with nucleotides, receptors, regulators, and effectors. In support of this concept, Gα subunits containing the two most common substitutions, QL and QP, exhibit important differences from one another with respect to dissociation from Gβγ and activation of effectors (15). Additionally, emerging studies of RAS show that different GTPase-deficient mutations, including of the corresponding glutamine, confer very different rates of intrinsic and GAP-stimulated GTP hydrolysis, intrinsic and stimulus-dependent nucleotide exchange rates, as well as distinct downstream effector selectivity profiles (14, 16–18).

Mutations of the catalytic glutamine are routinely used to stabilize the GTP-bound state of Gα, and by extension to reveal the biological importance of a given G protein subtype. Pioneering investigations used glutamine-to-leucine, and to a lesser extent glutamine-to-proline, mutations to demonstrate the oncogenic potential of $G\alpha_o$, $G\alpha_{12}$, $G\alpha_{13}$, and $G\alpha_z$ in cultured cells (19–23). Here, we considered other G protein subtypes and alternative glutamine substitutions, most of which are not associated with disease phenotypes. Through a systematic comparison of all possible substitutions, in multiple isoforms of Gα, and in multiple organisms, we determined that the catalytic glutamine is part of an allosteric pipeline that links receptor activation to subunit dissociation. Rather than existing in either an “on” or “off” state, the G protein can form an ensemble of active states, a subset of which are still sensitive to receptor regulation.

RESULTS

Catalytic glutamine mutations confer distinct Gα- and Gβγ-mediated signaling outputs

The catalytic glutamine is essential for the deactivation of G proteins (24, 25). This residue promotes GTP hydrolysis by positioning a water molecule for nucleophilic attack on the γ-phosphate of GTP (10). The glutamine is located at the beginning of the Switch II region of Gα, which upon activation adopts a helical conformation that displaces Gβγ and enables the high-affinity binding of effectors (26). Thus, whereas all mutations at this site should lead to a deficiency in GTPase activity, we postulated that different substitutions would evoke distinct changes in Switch II that also differed in their ability to bind to Gβγ and activate effectors. Because the $G\alpha_{q/11}$ Q209L and Q209P mutants are most commonly found

in uveal melanoma (COSMIC v94), these mutations in particular may possess structural and functional properties that favor the growth of the host cell.

To determine whether mutations found at the catalytic site were functionally distinct, we compared the ability of all possible glutamine mutations to alter the coupling of known binding partners and regulators of Gα subunits. We initially used the *Saccharomyces cerevisiae* (yeast) model system. In contrast to the tremendous diversity of mammalian signaling pathways, yeast has just one canonical GPCR, one RGS protein, and one G protein and therefore offers a highly tractable and well-characterized signaling system (Fig. 2A). First, we examined the functional consequences of Gα binding to the phosphatidylinositol 3-kinase Vps34, which is required for autophagy (27, 28). We previously showed that $Gpa1^{Q323L}$ is a strong inhibitor of nutrient-driven autophagy (29). To determine whether other GTPase-deficient mutants shared this property, we measured autophagy in wild-type cells expressing the biosensor Rosella and a plasmid-borne copy of wild-type (WT) Gpa1 or one of 19 glutamine mutants, in nitrogen-deficient medium (29, 30). Expression of an extra copy of WT Gpa1 (not activated) in otherwise WT cells increased autophagy slightly. In contrast, and as shown previously, the Gpa1 QL mutant attenuated the response (29) as did the QE, QA, QI, and QY mutants (Fig. 2, B and C). The other substitutions had little or no effect. These data suggest that catalytic glutamine mutations have substantial differences in their ability to regulate the effectors of Gpa1-GTP.

Mutants that lack GTPase activity are likely to bind to GTP, but a subpopulation might nevertheless remain bound to GDP and Gβγ (31). As an initial test of this, we used a transcription-reporter assay that depends on the release of Gβγ (32). Expression of a plasmid-borne copy of wild-type Gpa1 decreased basal transcriptional activity, indicating that it could sequester Gβγ (Fig. 2, D and E). Several of the mutants displayed a concentration-response curve similar to that of wild-type Gpa1, indicating that these also associated with Gβγ. In contrast, most of the mutants that we tested, including QP, increased basal transcriptional activity, presumably by enhancing the ability of the receptor to activate the wild-type endogenous Gα protein. This could possibly be achieved by simultaneous coupling of wild-type and mutant Gα proteins to the receptor dimer (33–36). These data indicate that some mutants promoted Gβγ dissociation and activation and did so in a genetically dominant manner. We observed a similar response profile in cells lacking the RGS protein Sst2 (fig. S1). Thus, our experiments showed that catalytic glutamine mutations produced various levels of signaling through Gα– and Gβγ-mediated pathways, whereas RGS binding was unaffected in the yeast signaling system. Whereas some glutamine mutants led to Gα-mediated inhibition of the autophagy pathway, others enhanced the response. Some mutants sequestered Gβγ, whereas others triggered sustained release of Gβγ. Together, these data revealed the existence of multiple distinct forms of “constitutively active” Gpa1.

Catalytic glutamine mutations confer substitution- and subtype-specific activation by mammalian GPCRs

We next considered the function of catalytic site mutations in the human G proteins $G\alpha_q$, $G\alpha_s$, and $G\alpha_{i3}$. To that end, we used bioluminescence resonance energy transfer (BRET)

to measure the association of Gα with Gβγ in HEK293 cells cotransfected with a plasmid encoding the neurotensin receptor 1 (NTR1) (37). As expected, the $G\alpha_q$ mutants bound poorly to Gβγ, and consequently responded poorly to the stimulus (Fig. 3, A and B). In contrast to $G\alpha_q$, the $G\alpha_s$ mutants bound nearly as well to Gβγ as did the wild-type protein under basal conditions, and in most cases responded to stimulus as well as or better than the wild-type protein (Fig. 3, C and D; fig. S2). To our surprise, many of the mutations conferred on $G\alpha_s$ the ability to respond to neurotensin through NTR1, a receptor to which it is not predominantly coupled (38, 39). Finally, we observed a third pattern for $G\alpha_{i3}$, whereby a subset of mutant subunits was activated by neurotensin, whereas others were not (Fig. 3, E and F). This effect appeared to be independent of the receptor used, because we obtained a largely similar response with the μ-opioid receptor (MOR) when activated with DAMGO (fig. S2). These data indicate that the GTPase-deficient mutants could still bind to Gβγ and could still be activated by receptor ligands. Thus, each glutamine mutant responded differently to the same activated receptor, suggesting that each mutation confers distinct changes in regions of Gα that contribute to receptor coupling. For some $G\alpha_s$ mutants, these changes conferred the ability to respond to neurotensin (Fig. 3, C and D) (40, 41). Conversely, we showed that signaling by $G\alpha_q$ and $G\alpha_{i3}$ mutants was attenuated after the addition of the receptor allosteric modulator SBI-553 (Fig. 3, G to I; fig. S2) (42). Thus, some mutationally activated forms of Gα could be further activated—and inactivated—by receptor ligands.

Catalytic glutamine mutations confer substitution- and subtype-specific interaction with Gβγ

We then considered the main structural components contributing to mutation-specific differences in receptor-mediated G protein subunit dissociation. There are two major Gβ-binding sites in Gα (Fig. 4A): the N terminus, which is absolutely required for Gβγ binding, and Switch II, which is at the interface between Gα and Gβγ (43–45). The strengths of the interactions in these two binding sites should correlate with Gβγ dissociation, as was determined experimentally (Fig. 3, A to F) (26). We calculated the interaction energy between $G\alpha_i$ and Gβγ subunits [averaged over the molecular dynamics (MD) simulation trajectories for wild-type $G\alpha_i$ and selected mutants]. The Gα and Gβγ interaction energies showed that, of these two regions, the Switch II–based interactions exhibited more variation among the mutants (Fig. 4, B and C). These results indicate that the catalytic glutamine, like Switch II, could promote Gβγ dissociation. We postulate that Gln^{204} is involved in allosteric communication mechanisms that link receptor activation to the dissociation of $G\alpha_i$ from Gβγ. For other Gα subtypes tested, Switch II interactions with Gβ may play a less important role because most glutamine mutants displayed weak receptor-mediated Gβγ dissociation.

To provide mechanistic insights into the disparate behaviors of Gln^{204} mutants in $G\alpha_i$ as compared with the corresponding Gln^{209} in $G\alpha_q$, we turned to MD simulations. The dynamic nature of the Gα interface with Gβγ suggested that there may be correlated residue motions that promote allosteric communication between the residues in $G\alpha_i$, and possibly in $G\alpha_q$, located in the interface with Gβγ and with GPCRs. To that end, we used the Allosteer method (46–49), which uses statistical correlation in residue movements to calculate the

pipeline of residues involved in allosteric communication between stipulated regions in the protein structure.

Allosteer also calculates the allosteric communication strength between these stipulated regions. The allosteric "hub score" is a calculated quantity that denotes the strength of contribution by each residue located in the allosteric communication pipeline within Gα. This analysis revealed the allosteric communication pipelines for $G\alpha_i$ and $G\alpha_q$, initiated from the residues in the Gβγ interface passing through the nucleotide-binding site residues and ending with residues in the GPCR interface (Fig. 4, D to F and table S4). The allosteric communication pipelines in $G\alpha_i$ appeared to be stronger than those in $G\alpha_q$. In addition, the allosteric hub score for the catalytic glutamine was higher in $G\alpha_{i1}$ than in $G\alpha_q$.

Our results indicated that the catalytic glutamine in $G\alpha_{i1}$ may play a role in mediating the allosteric communication from the Gβγ interface through the nucleotide-binding site to the C-terminal α5 helix tip. Mutating Gln^{204} to other amino acids may therefore have effects on regions located in the allosteric communication pipeline, including the Switch II region, in $G\alpha_{i1}$. The allosteric communication strength between Gln^{204} and Switch II may, in turn, partially explain why different substitutions in $G\alpha_i$, but not in $G\alpha_q$, had distinct receptor-mediated Gβγ dissociation profiles. Together, these data indicate that some mutants retained the ability to bind to Gβγ and receptors, and did so in a manner that was substitution- and subtype-dependent. Furthermore, these data revealed that there is an underappreciated contribution of the catalytic glutamine in allosteric communication leading to receptor-mediated Gβγ dissociation.

Biophysical characterization of glutamine mutants

Whereas all glutamine mutants should exhibit attenuated GTPase activity, they are not necessarily all GTP-bound. Indeed, results from our BRET experiments indicated that some of the mutants could still be stimulated by GPCRs. To determine how they adopt an active state, we purified mutants with substitutions most commonly found in Gα-driven cancers (leucine, proline, arginine, and tyrosine) (COSMIC v94). In addition, these substitutions represent three of the four categories of side-chain properties (charge, size, and hydrophobicity). We also included a fifth substitution as representative of polar, noncharged residues (asparagine). For these and other biophysical experiments, we used $G\alpha_i$ because it is the only subtype for which there is an x-ray structure and NMR assignments in the GDP-, apo-, and GTPγS-bound states (45, 50–52).

To verify that the catalytic glutamine was necessary for GTP hydrolysis, we purified wild-type and the five mutant forms of $G\alpha_{i1}$ in the presence of GDP. We then combined each with GTP conjugated to the BODIPY fluorophore and monitored fluorescence over time (53). All six proteins bound to GTP, as indicated by the rapid increase in fluorescent signal (Fig. 5A). Whereas the wild-type protein exhibited a subsequent reduction in signal, owing to the lower quantum yield of the hydrolysis product, the mutant proteins did not. These data indicate that all five mutants had substantially impaired GTPase activity.

Next, we tested the ability of each mutant to undergo nucleotide exchange, by loading $G\alpha_{i1}$ with GDP and measuring the increase in fluorescence on binding to BODIPY-GTPγS (54).

The mutants exhibited a range of exchange rates, with most exchanging faster than the wild-type (Fig. 5B). The fast intrinsic exchange of most mutants suggests that nucleotide binding was destabilized. That some mutants were fast exchangers would explain why they were poorly activated by receptors in cells. However, one of the mutants, QY, exchanged more slowly than the wild-type and yet was unaffected by receptor stimulation (Fig. 3F). Thus, there was no strict correlation between receptor-induced and intrinsic nucleotide exchange rates.

Because Gα subunits were shown to function as pH sensors that can be regulated by proton binding, we examined whether Gα mutants underwent pH-dependent nucleotide exchange (55). The wild-type protein exchanged somewhat more rapidly at pH 6 than at pH 7, as did the other fast-exchanging mutants; in contrast, the QY mutant exchanged more slowly (Fig. 5C). Thus, the G protein mutants were differentially regulated, and sometimes opposingly, by proton binding.

To determine whether the differences in the intrinsic nucleotide exchange rates were caused by unique preferences of these mutants for GTP, we measured the dissociation of BODIPY-GTPγS in the presence of excess unlabeled GTPγS (Fig. 5D). Our results showed that the QP mutant had a faster dissociation rate than that of the wild-type, indicating that this mutant bound more poorly to GTPγS. Other mutations, such as QL, QN and QR, conferred a more modest increase in GTPγS dissociation rate relative to that of the wild-type. In this assay, QY was again an outlier, exhibiting a dissociation rate that was considerably slower than that of the wild-type. Whereas these mutants were all GTPase-deficient, they had different exchange and dissociation kinetics. These differences likely reflect the existence of conformationally distinct states of activation.

Nucleotide exchange (GDP to GTP) results in conformational rearrangements, which are critical in maintaining the structural integrity of the active state and the cooperativity of the switches (8, 45). To test whether the mutants underwent distinct conformational rearrangements, we measured protein unfolding as a function of increasing temperature with the SYPRO Orange dye. This dye has an increased quantum yield when bound to hydrophobic areas, such as those that become more prominent during protein unfolding (56). As reported previously, wild-type $G\alpha_{i1}$ was considerably more thermostable when bound to GTPγS than when bound to GDP (Fig. 5E) (57), consistent with the more rigid conformation of the active state. In the GDP-bound state, all of the mutants had a melting temperature (T_m) value similar to that of the wild-type. However, in the GTPγS-bound state, the QP mutant showed a 7°C destabilization, whereas the QL, QN, and QR mutants showed a 3 to 4°C destabilization (Fig. 5, F to H; table S1). The QY mutant was destabilized in comparison to the wild-type, with a 15°C shift in Tm, in the active state (Fig. 5I; table S1). Whereas these mutations led to a range of destabilization trends in the active state, there were also differences in the cooperativity of the unfolding patterns. Some mutants, such as QP and QY, showed more cooperative unfolding patterns, whereas the QL, QN, and QR mutants showed less cooperative unfolding patterns, in comparison to that of the wild-type. These data indicate that some mutations disrupted the cooperative stability provided by the switch regions.

Our thermostability data revealed mutation-specific differences in Switch II, which propagated throughout the protein, leading to differences in the cooperativity of unfolding. Gα is a two-domain protein, consisting of a RAS-like domain and an all-helical domain. The cooperativity of unfolding of Gα is dependent on both of these domains. To increase the sampling of this two-domain protein and further analyze the cooperative unfolding of some mutants, we used near-UV circular dichroism (CD) to confirm our Tm measurements (fig. S3 A–E), as well as to analyze changes in secondary structure during thermal unfolding. Wild-type $G\alpha_{i1}$ had considerable α-helical content, as indicated by the pronounced peak at 190 to 230 nm (Fig. 5J; fig. S3 F and G), and this signal is derived from the all-helical domain and a portion of the RAS-like domain. The QL, QP, and QR mutants showed a decrease in β-sheet content relative to that of the wild-type, suggesting a loss of interactions that stabilize the β-sheet structure within the RAS-like domain. Conversely, the QN and QY mutants showed a decrease in α-helical content, with no corresponding changes in β-sheet content (Fig. 5K; fig. S3 H and I). These results demonstrated that each of the mutants exhibits distinct secondary structural content and conformational rearrangements on binding to GTP.

Structural analysis of the glutamine mutants

To more fully understand how the glutamine mutations affect $G\alpha_{i1}$ structural dynamics, we applied two-dimensional heteronuclear single-quantum coherence (HSQC) NMR. Unlike other biophysical techniques, such as X-ray crystallography, NMR reports site-specific changes in protein structure and conformational dynamics on multiple timescales. Two dimensional ^{1}H-^{15}N HSQC spectra enable the detection of protons directly bonded to a ^{15}N nucleus, including both backbone and side-chain NH resonances. These spectra are highly informative, because they contain a “fingerprint” of the protein backbone, enabling site-specific changes to be detected through shifts in peak intensity (line broadening) or peak position relative to the assigned wild-type (chemical shift perturbation). Furthermore, changes in dynamics can be inferred from the broadening or loss of peaks in the spectrum (undetected peaks). We obtained HSQC spectra for ^{15}N-enriched wild-type and selected glutamine mutants and compared their spectra to identify residue-specific differences. We used previously published backbone assignments for GDP- and GTPγS-bound wild-type $G\alpha_{I}$ (51, 57, 58).

We began with the QL mutant because it is the best-characterized of the glutamine variants and there is a low-resolution crystal structure available (50). The wild-type spectrum of ^{15}N-enriched $G\alpha_{i}$-GTPγS had 310 NH detectable peaks of 321 observable NH peaks (Fig. 6A). We transferred 82% of these assigned peaks using published assignments of $G\alpha_{i}$-GTPγS (57). Conversely, the QL-GTPγS HSQC spectrum showed additional peaks, with 372 detectable NH resonances. These observations suggest that the QL mutant may adopt an additional conformation detectable by NMR. Moreover, approximately 60 of these peaks were shifted relative to the wild-type-GTPγS spectrum (Fig. 6A). These shifts correspond to resonances associated with β2, β4, β5, α5, and Switch II regions (Fig. 6B, red regions) within the RAS-like domain. Moreover, comparison of the HSQC spectrum of QL-GTPγS (Fig. 6A, black) with the wild-type-GTPγS (Fig. 6A, red) revealed several resonances that were broadened in the QL spectrum (Fig. 6 B, magenta). For example, peaks from residues

of QL-GTPγS in Switch I (Gly^{183}) and the α5 helix (Ala^{338}) were broadened compared to the spectrum acquired for wild-type-GTPγS (Fig. 6B); we also examined the extent of broadening for each residue in the mutants with respect to the wild-type (fig. S4). The broadening of resonances in the spectrum suggested that the QL mutation may have altered $G\alpha_{i1}$ dynamics. Together, our analyses indicate that the QL mutation caused structural perturbations, predominately in the RAS-like domain, altered dynamics, and the formation of an additional state detectable by NMR.

To understand the nature of the conformational dynamics, we performed MD simulations on mutant and wild-type proteins bound to GTPγS. To validate the flexibility seen in the MD simulations, we calculated the change in RMSF for each residue going from the wild-type protein to the corresponding mutant and compared it to the peak broadening observed by NMR analysis. This comparison showed that MD simulations recapitulated the peak-broadening changes for 13 of 19 residues in the QL mutant (fig. S4B). To further understand the major domain motions, we performed principal component analysis (PCA) on the MD simulation trajectories of the wild-type and QL proteins. We projected the MD simulation snapshots on the top-weighted two PCs, PC1 and PC2. PC1 represents a twist motion between the RAS-like and helical domains, whereas PC2 represents domain separation at the hinge region of Gα. We prepared a population density map of the conformation ensemble from the MD simulations for QL (Fig. 6C). Whereas the dynamics of the wild-type protein showed one conformational minimum, the QL mutant showed greater flexibility, with two distinct minima, in accordance with the additional NH peaks observed by NMR. We identified the regions in $G\alpha_{i1}$ that showed conformational changes in the two distinct conformations of the QL mutant (fig. S4).

We then sought to determine the structural basis for functional differences exhibited by the QR and QP mutants. The HSQC spectrum of QR-GTPγS (purple) showed 100 fewer peaks compared to that of wild-type-GTPγS (red). Unlike the QL mutant, the QR mutant had few chemical shift perturbations (Fig. 6, D and E). The missing peaks included those from both the RAS-like and the all-helical domain, as well as at the domain interface (Fig. 6E). The large number of undetected peaks suggest that this mutant possesses altered conformational dynamics properties. MD simulations recapitulated the peak-broadening observed by NMR in the QR mutant (fig. S4B). The population density map from the MD simulations showed three major conformational minima for the QR mutant (Fig. 6F), indicating a highly dynamic system with respect to both PC1 and PC2. The large number of undetected peaks for the QR mutant may be a consequence of motions within and between the RAS-like and all-helical domains.

Finally, we compared the HSQC spectrum of QP-GTPγS (blue) with wild-type-GTPγS (red). In this case, the QP mutant (312 peaks) showed a number of peaks similar to wild-type (310 peaks), and there were a substantial number of resonances in QP that overlapped with the wild-type (Fig. 6G). The HSQC spectrum of QP showed that most resonance perturbations exhibited peak shifts, as opposed to resonance broadening. Most of the chemical shift perturbations corresponded to residues in important conserved nucleotide-binding motifs such as G-1 (in α1), and G-3 (in Switch II), G-4 (in α G), and the G-5 boxes (7). Residues in these nucleotide-binding motifs are involved in contacts with the

α, β, and γ phosphates, magnesium binding, and guanine base recognition within the RAS-like domain (Fig. 6H). The localized changes in these regions of QP may explain the fast nucleotide exchange kinetics and destabilization of the active state (Fig. 5, B to I). Analysis of the MD simulation trajectories showed the dynamics of the residues in the nucleotide-binding region through their contribution to PC1 of the QP mutant compared to wild-type (fig. S5, A to C). Thus, the HSQC spectrum for QP was distinct from those of QL and QR. The new peaks for the QL mutant suggested that it may exist as two (or more) conformeric states. In contrast, new peaks were not observed for the QP mutant. Rather, the population density map for the MD simulation–generated conformational ensemble showed one densely populated basin close to the wild-type and a sparsely populated wider sub basin along the PC2 axis (Fig. 6I). The overlay of major basins between QP and the wild-type is consistent with our NMR analysis, and showed substantial overlap between the two proteins. In particular, MD simulations recapitulated the peak-broadening changes for 16 of 19 residues observed by NMR. Moreover, the flexibility of the residues in the RAS-like domain, as quantified by their RMSF values calculated from MD simulations of the QP and QL mutants, was higher compared to the all-helical domain (fig. S5, B to D); this may partially explain the chemical shift perturbations observed predominantly in the RAS-like domain for the QL and QP mutants. Thus, each of the mutants appeared to have a unique structure, and the QP mutant was the mutant most similar to the wild-type.

In summary, NMR measurements combined with PC analysis of MD simulation trajectories revealed unique conformational dynamics in the Gα mutants, with respect to PC1 and PC2. The QL mutant populated two minima, one with an interface similar to that of the wild-type and the other, more densely populated, basin with a slightly shifted interface and broken interactions between Switch III and the all-helical domain (fig. S5, E and F). In contrast, the QR mutant had three equally populated conformations, suggesting a considerably higher degree of flexibility than that of either QL or QP. The major movement of QR along the PC2 axis signified domain separation and the uncoupling of the domain interface. The higher flexibility of QR was evident in the loss of more than 100 peaks in the NMR spectrum. The QR mutant also displayed movement along the PC1 axis, which suggested that this mutant also adopts new interfaces. Due to the high flexibility, we likely cannot capture these new conformations on the NMR timescale. The ability of the QR mutant to simultaneously separate the domains and adopt new conformations may account for the fast exchange kinetics, while still maintaining a relatively high thermostability in the active state (Fig. 5G). Finally, the QP mutant displayed movement only along the PC2 axis, with one densely populated basin close to the wild-type basin. In conclusion, each of the mutants tested showed conformational heterogeneity and dynamics in the active state. Whereas the QP mutant was the most similar to wild-type, other mutants, such as QL and QR, adopted previously uncharacterized conformers. Thus, a GTPase-deficient mutation does not necessarily confer a wild-type–like, GTP-bound state as was previously thought.

Catalytic glutamine mutations confer distinct Gα-mediated signaling outputs in mammalian cells

Our biochemical and biophysical analysis revealed an unexpected plasticity in each of the glutamine mutants. Rather than being permanently locked in a single, static and fully

activated state, each of the mutants was distinct and structurally dynamic. The structural differences are highlighted by our CD, NMR analysis, and MD simulations. Our BRET measurements provided evidence for functional differences in receptor coupling and subunit dissociation. Our next goal was to determine whether these differences in structure and subunit dissociation led to differences in the coupling of Gα to effectors. To that end, we first tested the activation of the extracellular signal–regulated kinase (ERK) signaling pathway by measuring induction of the serum response element luciferase transcriptional reporter (SRE-luc). HEK293 cells were transfected with the SRE-luc construct, Renilla control, and plasmids encoding each of the five mutants or wild-type $G\alpha_q$. The QP and QY mutants induced increased transcriptional activity compared to that induced by the wild-type control, whereas the QL and QR mutants showed intermediate transcriptional activity. Surprisingly, the QN mutant showed no response, similar to that seen for the wild-type protein, presumably because it was poorly expressed (Fig. 7A; fig. S6). Thus, mutating the catalytic glutamine did not always result in pathway activation, even when the G protein is considered to be constitutively active.

The varied transcriptional responses may indicate differences in the effector coupling, or "pathway specificity," of the catalytic glutamine mutants. Although $G\alpha_q$ signals through its effector phospholipase Cβ (PLCβ) to activate the canonical ERK pathway and to initiate tumor formation, studies showed that $G\alpha_q$ also signals through a noncanonical signaling axis mediated by the RhoGEF TRIO, leading to the activation of focal adhesion kinase (FAK) to control aberrant cell growth (59). Indeed, the QL, QP, QR, and QY mutants all activated the FAK pathway, but had distinct effects on ERK activity (Fig. 7, A to D), mirroring the results obtained from the transcriptional response experiments. The QN mutant did not activate either the ERK or the FAK pathway and instead showed a response similar to that of wild-type $G\alpha_q$. These data suggest that not all of the catalytic glutamine mutants are properly expressed and that they may fail to activate pathways involved in aberrant cell growth.

Thus far, we showed that most mutations intrinsically activated $G\alpha_q$-driven downstream pathways. Our BRET data indicated that some mutants could be further activated by GPCRs (Fig. 3, A and B). In light of these results, we tested whether further GPCR activation of the glutamine mutants resulted in distinct functional activity in the cell. To that end, we used HEK293 cells that expressed a subset of glutamine mutants and a synthetic $G\alpha_q$-coupled GPCR ($G\alpha_q$ DREADD) that is activated by a pharmacologically inert ligand, clozapine N-oxide (CNO) (60). Most glutamine mutants intrinsically activated downstream signaling under basal conditions, as expected, but were not further activated upon the addition of CNO (Fig. 7E). Whereas the QN mutant did not show intrinsic pathway activation, it showed robust activation of downstream signaling pathways after CNO addition. Thus, even a poorly expressed mutant could be activated by receptors.

Having determined that the glutamine mutants showed increased, albeit varied, intrinsic and GPCR-mediated pathway activation, we next considered whether these observations directly translated to enhanced cell proliferation or proliferative potential. To test this, we co-transfected NIH3T3 cells with plasmids encoding $G\alpha_q$ wild-type or glutamine mutants and GFP, and then measured the amounts of the nuclear protein Ki67, which is used

as a marker for cell proliferation (61). We found that the QR and QN mutants behaved similarly to wild-type $G\alpha_q$, whereas the QL, QP, and QY mutants resulted in considerably increased cellular proliferation. These findings revealed that GTPase deficiency in Gα does not necessarily determine the constitutive activation of signaling pathways, and that we cannot assume a strict correlation between constitutive activity and cellular proliferation. More broadly, we conclude that the various glutamine mutants exhibit distinct structural and molecular properties, and these are manifested in distinct cell signaling behaviors.

DISCUSSION

Large genome sequencing campaigns, such as those performed by The Cancer Genome Atlas, have provided new and surprising information about the contribution of G protein mutations to cancer and other diseases (12). In uveal melanoma, mutations in $G\alpha_q$ or $G\alpha_{11}$ are commonly observed (13). These mutations are almost always at the catalytic glutamine site, and this residue is almost always replaced with leucine or proline. Moreover, mutations at Gln^{209} are much more prevalent than those at Arg^{183}, even though both sites are important for GTPase activity. Other G protein isoforms are rarely affected, although mutations in $G\alpha_s$ and $G\alpha_{i2}$ are present in some cancers (62–64). Thus, there appears to be a strong genetic selection for two of nineteen possible substitutions, at one of two amino acids important for catalysis, in just two of sixteen Gα subtypes, and in just one of multiple cell types in the human body.

To understand the broader functional relevance and to uncover additional roles of the catalytic glutamine, we measured multiple functional outputs, for multiple G protein subtypes, in yeast and animal cells, for all possible replacements of the active site residue. We conducted a broad array of cell signaling assays (BRET, effector activation, transcriptional induction, and cell proliferation), as well as molecular analyses (nucleotide binding, thermostability, CD, NMR and MD simulations). We profiled the most commonly occurring mutant forms of Gα and, just as importantly, mutants that occur rarely and may be incompatible with sustained cell growth. Depending on the specific substitution and the specific subtype of the G protein examined, changes at the catalytic glutamine resulted in distinct and sometimes opposing outputs. Whereas most of the mutants were constitutively active, some were inactive, and others were activated by receptors (including a receptor to which they do not predominantly respond). These differences were unexpected because it had been widely assumed that loss of GTPase function confers a singular, GTP-bound, fully activated form of the protein. Additionally, there are differences in the prevalence of individual mutations that may be due to unequal codon usage, phenotypic selection, or the environmental origins (as yet uncharacterized) of mutagenesis. Thus, whereas G proteins have long been regarded as simple on-and-off switches, our findings reveal that they adopt multiple functional states and that different activating or deactivating mutations populate a subset of those states.

In support of the model, our NMR studies revealed considerable diversity in protein structure and dynamics; whereas all glutamine mutations tested here shifted the equilibrium toward the active state, they did so in multiple distinct ways. We showed further that the GTP-bound state of a G protein α-subunit was an ensemble of active state conformations,

rather than a single conformational state, and that these conformations differed among the various glutamine substitutions. Whereas the QR substitution affected the helical and RAS-like domains, the effects of other substitutions were concentrated at the RAS-like domain, including nucleotide-binding motifs, or G-boxes, and Switch II. We showed further that the catalytic glutamine has a noncatalytic role in mediating allosteric communication between the receptor, nucleotide-binding pocket, and Gβγ subunits. Finally, our MD simulation analyses showed stronger involvement of the catalytic glutamine in allosteric communication within $G\alpha_i$ as compared to $G\alpha_q$. Thus, our analysis reveals important roles for the conserved glutamine in regulating protein structure and function, beyond its established role in catalysis. These functional effects include alterations in receptor coupling, and they differ substantially among G protein subtypes. The ensemble of states resulting from mutations also led to different patterns in downstream signaling.

In the long term, our findings have the potential to guide new pharmacology. One approach is to target the G proteins directly (65–67). In contrast to protein kinases, however, the high affinity of Gα subunits for their substrate nucleotide precludes the development of effective competitive inhibitors of GTP binding. This, combined with the high concentration of GTP in the cell, makes it unlikely that successful competition with a nucleotide analog can be achieved (68). A potential alternative is to develop compounds that allosterically inhibit GDP release or GTP binding, in opposition to receptors that act allosterically to promote nucleotide exchange. Attention has focused on two natural products with the desired activity. YM-254890 and FR900359 are cyclic depsipeptides, isolated from the bacterium *Chromobacterium sp*. and the plant *Ardisia crenatasims*, respectively. YM-254890 inhibits $G\alpha_q$ by allosterically stabilizing the protein in the GDP-bound form, preventing nucleotide exchange, and locking it in the inactive state (69, 70). FR900359 inhibits receptor-dependent activation of the G protein, and appears to do so in a long lasting or “pseudo-irreversible” manner (71, 72). FR900359 suppresses the hallmark features of malignant melanoma in cells and in animals expressing $G\alpha_q^{Q209P}$ and $G\alpha_{11}^{Q209L}$, and inhibition occurs within minutes after administration (59, 71, 73, 74). Our identification of putative allosteric druggable sites, some of which are unique to G protein subtypes, could lead to the identification of additional subtype-selective inhibitors of G protein activation. A third alternative, one that also emerged from our analysis, is to target cell surface receptors. In particular, we showed that a subset of Gα mutants retained some element of agonist-dependent activation and could also be inhibited by a receptor allosteric modulator. Thus, our efforts establish a biochemical basis for sorting specific mutations into functional subclasses, which could inform future laboratory-based or clinical studies and enable the stratification of cancer patients into specific treatment groups. This would provide biological selection criteria for selecting agents that target one pathway or another and would also provide a set of testable hypotheses about the effect of each mutant on cellular signaling pathways.

MATERIALS AND METHODS

Cell lines

HEK293T cells (ATCC; CRL-11268) overexpressing human $G\gamma_9$-GFP2 and wild-type or mutant human Gα-Rluc8 donors were used for BRET assays. Cells were grown at 37°C in Dulbecco's Modified Eagle Medium (DMEM, Corning; 10–017-CV) with 1% dialyzed fetal bovine serum (FBS, GIBCO; A3382001). HEK293 cells used for transcriptional reporter assays and for Western blotting studies were grown at 37°C in DMEM (Sigma Aldrich; D6429) with 10% sterile-filtered FBS (Sigma Aldrich; F2442). NIH3T3 cells used for cell proliferation studies were grown at 37°C in DMEM with 10% sterile-filtered newborn calf serum (Sigma Aldrich; 4637). Cell lines were tested for contaminants with the Lonza MycoAlert Mycoplasma detection kit (Lonza; LT07–418). Yeast *Saccharomyces cerevisiae* strains BY4741 (MAT**a** *his3*Δ1 *leu2*Δ0 *met15*Δ0 *ura3*Δ0) *bar1*::KanMX (*bar1*Δ) or *sst2*::KanMX (*sst2*Δ) (Research Genetics; 95401.H2) were used for transcription-reporter and autophagy analysis. Cells were grown at 30°C in selective (SCD) medium, comprised of yeast nitrogen base without amino acids and without ammonium sulfate (1.7 g/l), ammonium sulfate (5 g/l), complete synthetic media powder (MP Biomedicals), and 2% dextrose.

Mutagenesis

Primestar Max (Takara Bio; R045B) mutagenesis was performed with primers containing 5 bp 5' of the codon and 20 to 30 bp 3' of the codon (see table S2).

Transcription

Pheromone-induced gene induction was monitored as described previously (32). Briefly, BY4741 *bar1*Δ cells cotransformed with the plasmids pRS423-pFUS1-lacZ (2μ, amp^R, *HIS3*+) and pRS316-GPA1 (wild-type or mutant) (CEN/ARS, amp^R, *URA3*+) were grown to an OD_{600} of ~ 1. Cells were treated with synthetic α factor for 90 min at 30°C and then treated with the substrate fluorescein di-β-D-galactopyranoside for 90 min. The fluorescein signal was quantified at 485 nm excitation and 530 nm emission with a Molecular Devices Spectramax M5 plate reader. Data were normalized as a percentage of the average fluorescence value of cells transformed with the empty vector. Data were fit to a three-parameter log agonist to response curve in GraphPad Prism 8.

Autophagy assay

Cytoplasm-to-vacuole autophagy was monitored as described previously (29, 30). Briefly, BY4741 *bar1*Δ cells cotransformed with the plasmids pAS1NB-DsRed.T3-SEP (2μ, amp^R, *LEU2*+) and pRS316-GPA1 (wild-type or mutant) were grown to an OD_{600} of ~1. Cells were then washed and resuspended with SCD medium lacking ammonium sulfate (SCD-nit). Background fluorescence was measured with medium without cells. Measurements were made with a black clear-bottom 96-well microplate (Corning; 3631) that was sealed to decrease evaporation (adhesive PCR plate seal, Thermo Fisher Scientific; AB0558). Measurements were made with a Molecular Devices SpectraMax M5 for 8 hours at 30°C. Fluorescence was measured every 30 min for super-ecliptic pHluorin (SEP) (488

nm excitation, 530 nm emission) and DsRed.T3 (543 nm excitation, 587 nm emission). Time-course data were generated by calculating the ratio of DsRed.T3 to SEP fluorescence and fit to a fourth-order polynomial model in GraphPad Prism 8.

TRUPATH bioluminescence resonance energy transfer

HEK293T cells (ATCC; CRL-11268) were used to measure receptor-mediated dissociation of Gα and Gβγ, as described previously (37). Cells were transfected with plasmids expressing $G\alpha_s$, $G\alpha_q$, or $G\alpha_{i3}$ fused to Renilla luciferase 8 (Rluc8), $G\beta_3$, $G\gamma_9$ fused to GFP, and either the NTR1 neurotensin receptor or μ-opioid receptor in a 1:1:1:1 ratio. The approximate cell density for transfection was 750,000 cells in 3 ml of medium. After transfection (approximately 12 to 16 hours), the cells were plated onto poly-D-lysine–coated, 96-well white clear bottom plates (Greiner Bio-one; 655098) in DMEM with 1% dialyzed FBS and then incubated overnight. The next day (12 to 16 hours later), the cells were washed twice with assay buffer [20 mM (4-(2-hydroxyethyl)-1-piperazineethanesulfonic acid) (HEPES), Hanks' Balanced Salt Solution, (pH 7.4)]. Rluc8 substrate (Coelenterazine 400a, 10 μl, Nanolight) was added per well at a final concentration of 5 μM. Cells were then incubated for 5 min in the dark. DAMGO (30 μl of 3X) or neurotensin agonist in drug buffer (contains assay buffer, 0.1% bovine serum albumin and 0.1% ascorbic acid) was added per well, which was then incubated for 5 min in the dark. Plates were read for luminescence for 1 s per well with a Mithras LB940 multimode microplate reader (395 nm excitation, 510 nm emission). The BRET ratio was determined by dividing the fluorescence by the luminescence (GFP/Rluc8). The receptor-catalyzed dissociation of the heterotrimer (net BRET) was measured by comparing the energy transfer from donor to acceptor and reported as ratios: GFP/Rluc8 per well – Basal BRET (GFP/Rluc8 at lowest dose of agonist) = Net BRET. The net BRET was plotted as the GFP/Rluc8 ratio as a function of ligand concentration and fit to a nonlinear regression log-inhibitor vs. response (three parameters) curve in GraphPad Prism 8. BRET experiments with SBI-553 (MedChemExpress; HY-125880) were performed as described earlier with minor modifications. After the cells were washed twice with 60 μl of assay buffer,15 μL of SBI-553 was added per well at a final concentration of 10 μM. After the addition of SBI-553, the cells were incubated at room temperature in the dark for 90 min. Rluc8 substrate (Coelenterazine 400a, 10 μl, Nanolight) was added per well at a final concentration of 5 mM. Cells were then incubated for 5 min in the dark. Neurotensin agonist (15 μl of 6X) in drug buffer (contained assay buffer, 0.1% bovine serum albumin) was added per well, which was then incubated for 5 min in the dark.

Expression and purification of $G\alpha_{i1}$

Protein purification was performed as described previously, with minor modifications (75). BL21DE3 RIPL cells were transformed with PET-SUMO $G\alpha_{i1}$ plasmids (75) and grown overnight until they reached saturation in 5 ml of LB medium with 50 mg/mL kanamycin. One liter of fresh medium was then inoculated with the 5-ml starter culture. Cells were grown at 37°C until they reached an OD_{600} of 0.6 to 0.8. Protein expression was induced by the addition of 400 μM isopropyl β-d-1-thiogalactopyranoside. The cell culture temperature was reduced to 18°C for overnight expression. Cell cultures were harvested by centrifugation for 1 hour at 1789*g* at 4°C. Cells were resuspended in phosphate buffer [25

mM KH_2PO_4, 25 mM K_2HPO_4, 300 mM KCl, 500 mM (tris(2-carboxyethyl)phosphine) (TCEP), 50 μM GDP, 50 μM $MgCl_2$] and then lysed by sonication on ice. Lysates were clarified by centrifugation at 716*g* for 1 hour at 4°C. Clarified lysate was poured onto a column containing 5 ml of Ni-NTA resin (Thermo Fisher Scientific; 88222) that had been equilibrated in phosphate buffer and then washed with 5 column volumes of phosphate buffer to remove nonspecific binding proteins. $G\alpha_{i1}$ was eluted by the addition of 6 column volumes of elution buffer (phosphate buffer + 250 mM imidazole). Eluent was dialyzed overnight in 4 l of phosphate buffer in dialysis membrane tubing (3.5 kDa cut-off) with 1 mg of ULP1 protease. Cleaved protein was collected the following day by reverse-nickel chromatography. Protein was further purified with a Sepharose anion-exchange Q-column (Hi-trap Q high performance column, Cytiva; GE17–1154-01) equilibrated with equilibration buffer [25 mM Na_2HPO_4 (pH 8), 50 μM $MgCl_2$, 100 mM NaCl] and the flowthrough was collected. Protein was eluted with 25 mM Na_2HPO_4 (pH 8), 50 μM $MgCl_2$, and 1 M NaCl.

Fluorescence spectroscopy

Fluorescence experiments were conducted with an LS55 luminescence spectrofluorometer (Perkin-Elmer). Fluorescence (498 nm excitation, 508 nm emission) was measured in 1-ml cuvettes with constant stirring with magnetic stir bars. Data were acquired through FL WinLab software (Perkin-Elmer) (53, 54). To measure BODIPY-GTP hydrolysis, $G\alpha_{i1}$ was preincubated with equimolar concentrations of GDP. Baseline fluorescence was collected with 83 nM BODIPY-GTP in 1 ml of hydrolysis buffer [20 mM TRIS/HCl (pH 7) and 10 mM $MgCl_2$]. BODIPY-GTP loading and hydrolysis were initiated by the addition of 10 μM $G\alpha_{i1}$ to 1 ml of hydrolysis buffer containing the fluorescent analog. To measure nucleotide exchange and dissociation, baseline fluorescence was collected with 83 nM BODIPY-GTPγS in 1 ml of exchange buffer (20 mM HEPES, 10 mM $MgCl_2$, and 10 mM dithiothreitol) at pH 6 and pH 7. Exchange was initiated by the addition of 5 μM $G\alpha_{i1}$. Fluorescence was measured until nucleotide exchange reached saturation. After saturation of exchange at pH 7, 400 μM GTPγS was added to initiate nucleotide dissociation. Fluorescence was measured until the signal reached a previously established baseline fluorescence. All fluorescence measurements were normalized and fit to nonlinear regression one-phase association and dissociation kinetic models in GraphPad Prism 8.

Thermal shift assay

Five μM $G\alpha_{i1}$ in assay buffer [20 mM Na_2HPO_4 (pH 7), 10 mM $MgCl_2$, 10 mM NaCl] was incubated with 50 μM GTPγS and 2X SYPRO Orange protein gel stain 5000x concentrate in DMSO (Thermo Fisher; S6650) (76). The protein-dye mixture was added to a 96-well PCR plate in 40-μl aliquots. Data were collected at 30°C to 90°C at 1°C increments in a QuantStudio 7 Flex System (Thermo Fisher Scientific) qPCR instrument. Fluorescence values were normalized and fit to Boltzmann sigmoidal curves in GraphPad Prism 8 (see table S1).

Circular dichroism, thermal melt, and spectrum analysis

For spectrum analysis, 5 μM $G\alpha_{i1}$ was exchanged with an Amicon ultracentrifugal filter (10 kDa cutoff; Millipore Sigma; UFC901024) into 10 mM $MgSO_4$, 500 μM TCEP and was

incubated in 100 μM GTPγS. A baseline datapoint was collected to subtract the background. Spectral analysis data points were collected at 30, 50, 70, and 90°C. CD (mdeg) data were collected at 185 to 260 nm at 0.5 nm increments with 1.25 s per timepoint. The mean residue ellipticity was calculated and plotted against the wavelength and used as input for the secondary structure prediction webserver BeStSel (77). For thermal melt, 5 μM $G\alpha_{i1}$ was exchanged into 10 mM $MgSO_4$ with 500 μM TCEP and then was incubated in 50 μM GTPγS. CD (mdeg) was collected at 208 and 222 nm and from 30°C to 90°C in 1°C/min increments. The buffer baseline was subtracted from the datapoints. The melting temperature (T_m) was obtained by nonlinear fitting of protein denaturation to the Gibbs-Helmhotz equation. Thermal melt data were then plotted as mean +/− SD in GraphPad Prism 8. All CD experiments were performed on a Jasco J-1000 Series Circular Dichroism Spectropolarimeter.

NMR sample preparation and spectroscopy

^{15}N-enriched wild-type and mutant $G\alpha_{i1}$ were produced by large-scale expression in BL21(DE3)-RIPL *E. coli* grown in M9 minimal medium containing 1 g/l $^{15}NH_4Cl$ (Cambridge Isotope Laboratories) as the sole source of nitrogen and purified as described earlier (75). ^{15}N-enriched $G\alpha_{i1}$ was exchanged into NMR buffer [20 mM K2HPO$_4$ (pH 7), 50 mM KCl, 5 mM dithiothreitol, and 5 mM $MgCl_2$] containing 5% (v/v) D_2O and concentrated to 100 to 200 μM. The protein sample was incubated with a 10-fold excess of GTPγS (1 to 2 mM). NMR spectra were acquired at 25°C on a Bruker Avance 850 MHz NMR spectrometer. Two-dimensional ^1H–^{15}N HSQC experiments were recorded with 1024 and 128 complex points in the direct and indirect dimensions, respectively, with 20 scans per increment and a recovery delay of 1.0 s. Spectra were processed with Bruker Topspin 4,1,1 and analyzed with Sparky (UCSF). Average ^1H-^{15}N chemical shift perturbations were calculated with the formula $\Delta\delta = [(\Delta^1HN)^2 + (\Delta^{15}N/5)^2]^{0.5}$ where Δ^1H and $\Delta^{15}N$ correspond to chemical shift changes associated with ^1H and ^{15}N resonances, respectively. PyMOL (https://pymol.org/2/) was used to generate all images of molecular structures.

Molecular dynamics simulations

All simulations performed in this study are listed in table S3. We performed all-atoms MD simulations on four $G\alpha_i$ subunit-GTPγS-Mg^{2+} systems (wild-type, Q204L, Q204R, and Q204P) with three random initial velocities for 800 ns each. The initial conformations for the four systems were prepared by homology modeling based on the Gi sequence acquired from Uniprot. We performed homology modeling with SWISS-MODEL by inputting the wild-type sequence or the three mutated sequences using the PDB ID 1GIA, an active Gi structure, as a template (78). The generated apo-state active form structures were aligned with PDB ID 1GP2, and the binding pose of GTPγS-Mg^{2+} was transferred from 1GP2 to acquire the active $G\alpha_{i1}$ −GTPγS-Mg^{2+} complexes. We also simulated NTR1-Gi and one NTR1-Gq system to gain insight into the BRET experimental data. The NTR1 receptor structure was modeled based on the existing cryoEM structure of NTR1 bound to the $G\alpha_{i2}\beta_1\gamma_2$ protein complex and the NTS1 peptide (residues 8 to 13) (PDB ID: 6OS9) in the canonical C-form. The cryo-EM structure is missing the α-helical domain of the G protein, as well as residues 11 to 56, 184 to 234, and 241 to 355. Thus, the full heterotrimeric G protein based on the x-ray structure of human $G\alpha_i$ bound to GDP was aligned with the

NTR1 bound to the NTS1 peptide with PyMOL (PDB ID: 1GP2). This structure was still lacking the last six residues of the C terminus of the $G\alpha_i$ protein and hence we modelled them with MAESTRO (Schrödinger, LLC). For Gq, the heterotrimeric $G\alpha_q$ (PDB ID: 3AH8) bound to an inhibitor YM-254890 was used. We modelled the $G\alpha_q$ protein with the SWISS-MODEL web server using the initial orientation of $G\alpha_i$ from PDB ID 1GP2. The resulting complex was then minimized with the MacroModel suite in Maestro-2015–4.2 (Schrödinger Release 2021–4: MacroModel, Schrödinger, LLC, 2021). The sidechain residues within 5 Å of either the peptide or the nucleotide were allowed to freely minimize, whereas backbone atoms were fixed with a 200 kcal/mol/$Å^2$ force constant. A similar minimization scheme was used for the NTR1:$G\alpha_i/\alpha_q$ interface. All sidechains within 5 Å of the interface were allowed to freely minimize, whereas the corresponding backbone atoms were fixed with a 200 kcal/mol/$Å^2$ force constant. The orientation of the nucleotide GTPγS was taken from the monomeric x-ray crystal structure of the $G\alpha_i$ (PDB ID: 1GIA). The bonding connectivity of the small molecule was determined with the Ligprep utility of SCHRODINGER (Schrödinger Release 2021–4: LigPrep, Schrödinger, LLC, 2021). Charges and topological parameters were derived with the CgenFF module of CHARMM (79). The obtained topology from CgenFF was given a low molecular penalty and hence we decided to proceed with the same. The NTR1-Gi/Gq systems were simulated for 400 ns with three random initial velocities. To study the early events of dissociation between the Gα and Gβ subunits, five $G\alpha_{i2}\beta_1\gamma_2$ trimer systems without NTR1 were prepared based on the NTR1-bound structure by removing NTR1 from the complex. Four $G\alpha_{i2}\beta_1\gamma_2$ systems without NTR1 were prepared based on the NTR1 structure by removing NTR1 from the complex. The five systems included wild-type-GDP, wild-type-GTPγS-Mg^{2+}, Q204P-GTPγS-Mg^{2+}, Q204D-GTPγS-Mg^{2+}, and Q204L-GTPγS-Mg^{2+}. The mutations were made and energy-minimized by Maestro according to the protocol described earlier. The trimer systems were simulated for 400 ns with three random initial velocities. We used CHARMM-GUI (79) to construct the simulation system based on the acquired complex structures with the CHARMM36m force field (80). The force field parameter for GTPγS was offered in the standard CHARMM force field library. The four Gi-GTPγS-Mg^{2+} complexes were immersed in a 90 $Å^3$ cubic TIP3 water box, and then the solvated system was neutralized with 0.15 M NaCl. The five Gαi$\beta\gamma$ trimer complexes were immersed in a 113 cubic $Å^3$ TIP3 water box, which was neutralized with 0.15 M NaCl. The two NTR1–G protein systems were solvated in 199 explicit lipid (palmitoyl oleoyl phosphatidylcholine, POPC) bilayer and water with the CHARMM-GUI web server (79). The total system was made up of ~135,000 atoms in a periodic box of roughly 90*90*170 $Å^3$. We then added sodium and chloride counterions, maintaining the salt concentration of the system at 0.15 M. We performed all of the simulations with the GROMACS 2019 package (81). The LINCS algorithm was applied to all bonds and angles of water molecules with a 2-fs time step used for integration. A cutoff of 12 Å was applied for nonbond interactions, and the particle mesh Ewald method was used to treat long-range van der Waals interactions (82). Each system generated from CHARMM-GUI first went through energy-minimization with the steepest descent method until the maximum force was <1000 kJ/mol/nm. The system was then slowly heated from 0 to 310 K in NVT ensemble during a 1-ns heating process. The temperature was maintained using the Nosé-Hoover thermostat (83). A harmonic position restraint of 5 kcal/mol-$Å^2$ was applied on all heavy atoms of protein and ligand during

the heating process. We further equilibrated the system in the NPT ensemble for 30 ns to gradually release the restraint from 5 to 0 kcal/mol-Å^2 with a 1 kcal/mol-Å^2 per 5 ns window. The constant pressure was maintained by the Parrinello-Rahman method when coupled to a 1-bar bath (84). The last frame from the equilibrium process was used as the initial conformation for production simulations. We used three random seeds to generate different initial velocities for the three production runs, which lasted for 800 ns for $G\alpha_i$ systems and 400 ns for the NTR1-G protein system. The last 200 ns of the three 800-ns production runs from the $G\alpha_i$ simulations were combined into a 600-ns trajectory for future analysis. In a similar fashion, the last 200 ns of the three 400-ns production runs from the NTR1-G protein simulations, and the last 200 ns of three 400-ns production runs from the $G\alpha_{i2}\beta_1\gamma_2$ trimer simulations were combined into a 600-ns trajectory for further analysis.

Principal component analysis

We performed principal component analysis (PCA) on the 600-ns trajectory of all four $G\alpha_i$ systems to study the differences in their dynamics. The Cα atoms of all four systems were removed and merged into a single 2400-ns trajectory for PCA, so that the results could be readily compared for all of the four systems. PCA was performed with the GROMACS *covar and anaeig* modules. The top two PCs occupied >55% of the cumulative covariance, which suggested that PC1 and PC2 were sufficient to describe the most dominant motion of all of the four systems. To compare the dynamics of the RAS domain from MDS to the NMR perturbation observed, we performed PCA on the Cα atoms in the RAS domain (residues 34 to 60 and 185 to 341). We then calculated the contribution of each of the Cα atoms of residues in the RAS domain to the PC1 eigenvalue (fig. S5).

Conformational clustering analysis

We showed the dominant motion occurring in the QL, QP, and QR mutants with PC1 and PC2 (fig. S4). Because the QL mutant showed a major change in the PC1 space and QP showed a major change in the PC2 space, the centroids of the QL and QP clusters were used as representative structures to illustrate the motion in the PC1 and PC2 spaces. We first clustered QL/QP/QR sampling points based on their PC1 and PC2 values and then performed clustering analysis with the sklearn module in Python (85). All sampling points were clustered by the agglomerative method by defining the number of clusters as two for QL and QP, and three for QR. The centroid structures for each cluster were selected by sklearn. These centroid structures for each conformation cluster for the wild-type and mutants were used for all structure-rendering figures. We aligned the centroid structures by helical domain to show the movement of the RAS-like domain. PC1 was dominated by a sheer motion centered at the hinge region between two domains (fig. S4), whereas PC2 was mostly the open-and-close motion that causes the nucleotide-binding site to open (fig. S4). Movies showing the motion of PC1 and PC2 are available in Supplementary Materials. The contacting residue pairs in each representative structure between the RAS domain and the all-helical domain (fig. S5A) were identified with “Get_contact” software (https://getcontacts.github.io/). In the contact analysis, the RAS domain was defined as residues 34 to 60 and 185 to 341. The all-helical domain ranged from residues 63 to 176.

RMSF analysis

To validate the MDS results, we performed root mean square fluctuation (RMSF) analysis and compared our results to residue peak-broadening extracted from the NMR analysis. The RMSF results generally agreed with the NMR broadening analysis (fig. S4). RMSF analysis was performed with the GROMACS rmsf module by selecting protein backbone N atoms. The RMSF was calculated per residue after aligning the trajectory with the initial conformation. The RMSF values were plotted as δRMSF (WT-mutant) with NMR broadening data (I_{mutant}/I_{WT}; fig. S4). Both δRMSF and NMR broadening are shown as binary states as to whether they were broadened or not. Red blocks indicate no broadening, and blue blocks indicate broadening. White blocks represent peaks missing from the NMR readout. For dRMSF, broadened residues were defined as residues that had less than average δRMSF (WT-mutant) from all residues. For NMR-broadening data, broadened residues were defined as residues that had an I_{mutant}/I_{WT} value of < 0.9. The comparison between RMSF and NMR broadening showed a general trend that high RMSF correlated with low NMR broadening or missing peaks in the broadening data. To further understand the difference in dynamics between the RAS domain and the all-helical domain, we separated the trajectory for the RAS domain (residues 34 to 60 and 185 to 341) and from that of the all-helical domain (residues 63 to 176). We then aligned the snapshots for each of these domains within their respective trajectories. Then, we performed the RMSF and RMSD analysis for each domain (fig. S5A)

Interaction energy analysis

The interaction energy between the Gα and Gβ interfaces was calculated from the 600-ns merged trajectories described earlier. There are two major protein-protein interfaces between the Gα and Gβ subunits: the Switch II region from Gα, which binds to the loop regions of Gβ, and the N terminus of Gα, which interacts with the β-sheet structures of Gβ. The interface interaction energy calculation was only performed on the pairs of residues that maintained more than 40% simulation time over the 600-ns trajectory. Get_contact (https://getcontacts.github.io/) was applied to calculate the contact frequency between residues in the two interface regions. The interaction energy was calculated as the sum of the van der Waals interaction energy and the electronic interaction energy. The calculation was performed with the GROMACS energy module and plotted as a bar graph to show the comparison among WT and mutant systems (Fig. 4, B and C).

Allosteer analysis

We applied in-house software called Allosteer to study the allosteric communication residue network to shed light on the noncatalytic role of Gln^{204} and especially its distinct roles in Gi and Gq. Allosteer was used to identify the allosteric communication pipelines starting from the Gα residues in the Gβγ interface (including both the N terminus and the Switch II region) through the nucleotide-binding site and ending in the Gα C terminus. Allosteer calculates the mutual information in torsional angle distribution for all pairs of residues in the trimeric Gs and Gi proteins. We thenused graphic theory to calculate the shortest pathway with the highest mutual information connecting distant pairs of residues. The number of allosteric communication pathways passing through each residue is defined as

a “hubscore” and this score is used to describe the strength of the residues in allosteric communication. To define the Gα residues located in the Gβγ interface, nucleotide-binding site, and the C terminus, we used the MDS trajectories to identify the list of residues in these interfaces. The contact frequencies between the Gα N terminus/Switch II region, Gβ, and Gα-GTPγS were calculated with get_contact (https://getcontacts.github.io/). The residues from Gα, which had >40% contact frequency with GTPγS or Gβ, were defined as nucleotide-binding site residues and Gα/Gβ-binding site residues, respectively. The last 10 residues in the Gα C terminus were defined as C-terminal residues. The detailed residue list is shown in table S4. The sum of the hubscores for every residue involved in the pipelines was used to evaluate the strength of the allosteric communications. We showed that the strongest pipelines went through regions of interest defined earlier for both Gi and Gq simulation. These are shown in Fig. 4, D and F, as red tubes; the radius of each tube was scaled by their sum of hub scores. The ratio of the hub score of Gi Gln^{204} and Gq Gln^{209} (Gln^{204} equivalent) was plotted as a bar graph in Fig. 4E to show the relative ratio of the hub score of Gq Gln^{209} to that of Gi Gln^{204}.

Luciferase assays

HEK293 cells were cotransfected with the Turbofect transfection reagent (Thermo Fisher; R0534) with pCEFL-3x-Flag-Renilla-luciferase and pGL4.33[luc2P/SRE/Hygro] (Promega; E1340) or pGL4.34[luc2P/SRF-RE/Hygro] (Promega; E1350), with pcDNA5-$Gα_q$ wild-type, mutant, or pCEFL-GFP control for 48 hours (86). For experiments with $Gα_q$-DREADD, HEK293 cells were co-transfected with pCEFL-3x-Flag-Renilla-luciferase, pGL4.33, pCEFL-HA-$Gα_q$-DREADD, and pcDNA5-$Gα_q$ wild-type, mutant, or pCEFL-GFP control (86). Cells were serum-starved overnight, and luciferase activity was assessed with a Dual-Glo Luciferase Assay Kit (Promega; E2920) according to the manufacturer’s instructions and read with a Spark multimode microplate reader (Tecan).

Western blotting

Extracts of yeast BY4741 *bar1*Δ, transformed with the plasmids pRS316-ADH1-GPA1 and pRS316-ADH1-GPA1-Flag (wild-type or mutants) (CEN/ARS, amp^R, *URA3*+) (table S2) (87), were resolved by 10% acrylamide gel electrophoresis and subjected to Western blotting, as described previously (26). Gpa1 was detected with mouse anti-Flag (Sigma-Aldrich; F3165, 1:3000) and horseradish peroxidase (HRP)-conjugated goat-anti-mouse (Jackson ImmunoResearch Laboratories; 62–6520, 1:10,000) antibodies, and visualized with the ECL-plus reagent (Life Technologies; 1705061) on a ChemiDoc Touch Imaging System (Bio-Rad). HEK293 cells were transfected with pCEFL-empty vector control and pcDNA5-$Gα_q$ wild-type or mutants with the Turbofect transfection reagent for 48 hours. Cells were serum-starved overnight, washed three times with cold 1X PBS, and lysed with 1X Cell Lysis Buffer (Cell Signaling Technologies; 9803) prepared with 1X Halt Protease and Phosphatase Inhibitor Cocktail (Thermo Fisher Scientific; 78440). Lysates were centrifuged at 4°C for 10 min at 14,000*g* and heated for 5 min at 98°C with 4X Laemmli Sample Buffer (BioRad Technologies; 1610747) prepared with 2-mercaptoethanol. Primary antibodies were diluted at 1:1000 unless otherwise stated: FAK (Cell Signaling Technology; 71433), phospho-FAK (Y397) (Cell Signaling Technology; 8556), p44/42 MAPK (Erk1/2) (Cell Signaling Technology; 4695), Phospho-p44/42 MAPK (Thr202/Tyr204) (Cell Signaling

Technology; 4370), β-actin (Cell Signaling Technology; 4970, 1:3000), $G\alpha_q$ (Santa Cruz Biotechnology; sc-393, 1:2000). Goat anti-rabbit IgG-HRP secondary antibody was diluted 1:30,000 (Southern Biotech; 4040–05). Western blots were developed with the Pierce ECL Western Blotting Substrate (Thermo Fisher Scientific; 32106) according to the manufacturer's instructions. Signals were quantified with ImageJ software (US National Institutes of Health).

Flow cytometric analysis of cell proliferation

NIH3T3 cells were co-transfected with pCEFL-H2B-GFP and pCEFL-empty vector control, pcDNA5-$G\alpha_q$ wild-type or mutants, at a 5:1 ratio of pCEFL-H2B-GFP to experimental vector with the Turbofect transfection reagent (Thermo Fisher Scientific; R0531) for 72 hr. Cells were serum-starved overnight before collection, at which point they were fixed with the Invitrogen eBioscience Foxp3/Transcription Factor Staining Buffer Set (Thermo Fisher Scientific; 50–112-8857) according to the manufacturer's instructions. Cells were stained with Zombie Aqua Viability Dye (BioLegend; 77143), Alexa Fluor 700 anti-mouse Ki-67 Antibody (BioLegend; 652420), and Alexa Fluor 488 anti-GFP Antibody (BioLegend; 338008). Samples were processed with a Novocyte Advanteon (Agilent Technologies) and analyzed with FlowJo software (FlowJo, LLC).

Statistical Analysis

Data are ± SD from three or more independent experiments with two or more measurements each. Pair-wise comparisons are presented as $*P < 0.05$, $**P < 0.01$, $***P < 0.001$, and $****P < 0.0001$ by one-way ANOVA. Data are fit to one phase exponential decay curves or Boltzmann sigmoidal curves, where indicated.

Supplementary Material

Refer to Web version on PubMed Central for supplementary material.

Acknowledgments:

We thank A. Palmer (University of North Carolina at Chapel Hill) for comments on the manuscript and K. Crowhurst (California State University Northridge) for providing the Gα plasmid construct and other materials for expression and purification, all of which accelerated our early progress on this project.

Funding:

This work was supported by grants from the NIH (R01CA257505 to J.S.G., R01GM117923 to N.V., R35GM134962 to S.L.C., and R35GM118105 to H.G.D.).

Data and materials availability:

TRUPATH/BRET reagents are publicly available from Addgene (1000000163). All other unique reagents generated in the study will be available without restrictions. The study did not generate new unique code. MD simulations full trajectories are available at https://welcome.gpcrmd.org/ (deposited as file numbers 1248–1258). NMR data will be made available on request.

REFERENCES AND NOTES

1. Wacker D, Stevens RC, Roth BL, How Ligands Illuminate GPCR Molecular Pharmacology. Cell. 170, 414–427 (2017). [PubMed: 28753422]
2. McCudden CR, Hains MD, Kimple RJ, Siderovski DP, Willard FS, G-protein signaling: Back to the future. Cellular and Molecular Life Sciences. 62 (2005), pp. 551–577. [PubMed: 15747061]
3. Buck LB, The Molecular Architecture of Odor and Pheromone Sensing in Mammals. Cell. 100, 611–618 (2000). [PubMed: 10761927]
4. Margolskee RF, Molecular Mechanisms of Bitter and Sweet Taste Transduction. Journal of Biological Chemistry. 277, 1–4 (2002). [PubMed: 11696554]
5. Arshavsky VY, Lamb TD, Pugh EN, G Proteins and Phototransduction. Annurev.physiol 64, 153–187 (2003).
6. Sprang SR, Invited review: Activation of G proteins by GTP and the mechanism of Gα-catalyzed GTP hydrolysis. Biopolymers. 105 (2016), pp. 449–462. [PubMed: 26996924]
7. Sprang SR, G protein mechanisms: insights from structural analysis. Annu Rev Biochem. 66, 639–678 (1997). [PubMed: 9242920]
8. Lambright DG, Noel JP, Hamm HE, Sigler PB, Structural determinants for activation of the α-subunit of a heterotrimeric G protein. Nature. 369, 621–628 (1994). [PubMed: 8208289]
9. Flock T, Ravarani CNJ, Sun D, Venkatakrishnan AJ, Kayikci M, Tate CG, Veprintsev DB, Babu MM, Universal allosteric mechanism for Gα activation by GPCRs. Nature. 524, 173 (2015). [PubMed: 26147082]
10. Sondek J, Lambright DG, Noel JP, Hamm HE, Sigler PB, GTPase mechanism of Gproteins from the 1.7-A crystal structure of transducin alpha-GDP-AIF-4. Nature. 372, 276–279 (1994). [PubMed: 7969474]
11. Berman DM, Wilkie TM, Gilman AG, GAIP and RGS4 are GTPase-activating proteins for the G(i) subfamily of G protein α subunits. Cell. 86, 445–452 (1996). [PubMed: 8756726]
12. Arang N, Gutkind JS, G Protein-Coupled receptors and heterotrimeric G proteins as cancer drivers. FEBS Lett. 594, 4201–4232 (2020). [PubMed: 33270228]
13. van Raamsdonk CD, Griewank KG, Crosby MB, Garrido MC, Vemula S, Wiesner T, Obenauf AC, Wackernagel W, Green G, Bouvier N, Sozen MM, Baimukanova G, Roy R, Heguy A, Dolgalev I, Khanin R, Busam K, Speicher MR, O'Brien J, Bastian BC, Mutations in GNA11 in uveal melanoma. N Engl J Med. 363, 2191–2199 (2010). [PubMed: 21083380]
14. Li S, Balmain A, Counter CM, A model for RAS mutation patterns in cancers: finding the sweet spot. Nat Rev Cancer. 18, 767–777 (2018). [PubMed: 30420765]
15. Maziarz M, Leyme A, Marivin A, Luebbers A, Patel PP, Chen Z, Sprang SR, Garcia-Marcos M, Atypical activation of the G protein Gαq by the oncogenic mutation Q209P. Journal of Biological Chemistry. 293, 19586–19599 (2018). [PubMed: 30352874]
16. Hunter JC, Manandhar A, Carrasco MA, Gurbani D, Gondi S, Westover KD, Biochemical and structural analysis of common cancer-associated KRAS mutations. Molecular Cancer Research. 13, 1325–1335 (2015). [PubMed: 26037647]
17. Hobbs GA, Wittinghofer A, Der CJ, Selective Targeting of the KRAS G12C Mutant: Kicking KRAS When It's Down. Cancer Cell. 29, 251–253 (2016). [PubMed: 26977877]
18. Smith MJ, Neel BG, Ikura M, NMR-based functional profiling of RASopathies and oncogenic RAS mutations. Proc Natl Acad Sci U S A. 110, 4574–9 (2013). [PubMed: 23487764]
19. Kroll SD, Chen J, de Vivo M, Carty DJ, Buku A, Premont RT, Iyengar R, The Q205LG(o)-α subunit expressed in NIH-3T3 cells induces transformation. Journal of Biological Chemistry. 267, 23183–23188 (1992). [PubMed: 1429665]
20. Voyno-Yasenetskaya TA, Pace AM, Bourne HR, Mutant α subunits of G12 and G13 proteins induce neoplastic transformation of Rat-1 fibroblasts. Oncogene. 9, 2559–2565 (1994). [PubMed: 8058319]
21. Wong YH, Chan JSC, Yung LY, Bourne HR, Mutant α subunit of G(z) transforms Swiss 3T3 cells. Oncogene. 10, 1927–1933 (1995). [PubMed: 7761094]

22. Vara Prasad M, Dhanasekaran N, GTPase deficient mutant of G13 regulates the expression of Egr-1 through the small GTPase Rho. Oncogene. 18, 1639–1642 (1999). [PubMed: 10102635]
23. Xu N, Bradley L, Ambdukar I, Gutkind JS, A mutant α subunit of G12 potentiates the eicosanoid pathway and is highly oncogenic in NIH 3T3 cells. Proc Natl Acad Sci U S A. 90, 6741–6745 (1993). [PubMed: 8393576]
24. Graziano MP, Gilman AG, Synthesis in Escherichia coli of GTPase-deficient mutants of Gsα*. Journal of Biological Chemistry. 264, 15475–15482 (1989). [PubMed: 2549065]
25. Masters SB, Miller RT, Chi MH, Chang FH, Beiderman B, Lopez NG, Bourne HR, Mutations in the GTP-binding site of G(sα) alter stimulation of adenylyl cyclase. Journal of Biological Chemistry. 264, 15467–15474 (1989). [PubMed: 2549064]
26. Knight KM, Ghosh S, Campbell SL, Lefevre TJ, Olsen RHJ, Smrcka A. v., Valentin NH, Yin G, Vaidehi N, Dohlman HG, A universal allosteric mechanism for G protein activation. Mol Cell. 81, 1384–1396.e6 (2021). [PubMed: 33636126]
27. Slessareva JE, Routt SM, Temple B, Bankaitis VA, Dohlman HG, Activation of the Phosphatidylinositol 3-Kinase Vps34 by a G Protein alpha Subunit at the Endosome. Cell. 126, 191–203 (2006). [PubMed: 16839886]
28. Schu P. v., Takegawa K, Fry MJ, Stack JH, Waterfield MD, Emr SD, Phosphatidylinositol 3-kinase encoded by yeast VPS34 gene essential for protein sorting. Science. 260, 88–91 (1993). [PubMed: 8385367]
29. Rangarajan N, Gordy CL, Askew L, Bevill SM, Elston TC, Errede B, Hurst JH, Kelley JB, Sheetz JB, Suzuki SK, Valentin NH, Young E, Dohlman HG, Systematic analysis of F-box proteins reveals a new branch of the yeast mating pathway. Journal of Biological Chemistry. 294, 14717–14731 (2019). [PubMed: 31399514]
30. Rosado CJ, Mijaljica D, Hatzinisiriou I, Prescott M, Devenish RJ, Rosella: A fluorescent pH-biosensor for reporting vacuolar turnover of cytosol and organelles in yeast. Autophagy. 4, 205–213 (2008). [PubMed: 18094608]
31. Majumdar S, Ramachandran S, Cerione RA, New insights into the role of conserved, essential residues in the GTP binding/GTP hydrolytic cycle of large G proteins. Journal of Biological Chemistry. 281, 9219–9226 (2006). [PubMed: 16469737]
32. Shellhammer JP, Pomeroy AE, Li Y, Dujmusic L, Elston TC, Hao N, Dohlman HG, Quantitative analysis of the yeast pheromone pathway. Yeast. 36, 495–518 (2019). [PubMed: 31022772]
33. Chinault SL, Overton MC, Blumer KJ, Subunits of a Yeast Oligomeric G Protein-coupled Receptor Are Activated Independently by Agonist but Function in Concert to Activate G Protein Heterotrimers *. Journal of Biological Chemistry. 279, 16091–16100 (2004). [PubMed: 14764600]
34. Overton MC, Blumer KJ, G-protein-coupled receptors function as oligomers in vivo. Current Biology. 10, 341–344 (2000). [PubMed: 10744981]
35. Gehret AU, Bajaj A, Naider F, Dumont ME, Oligomerization of the Yeast α-Factor Receptor: Implications for dominant negative effects of mutant receptors *. Journal of Biological Chemistry. 281, 20698–20714 (2006). [PubMed: 16709573]
36. Velazhahan V, Ma N, Pándy-Szekeres G, Kooistra AJ, Lee Y, Gloriam DE, Vaidehi N, Tate CG, Structure of the class D GPCR Ste2 dimer coupled to two G proteins. Nature. 589, 148–153 (2021). [PubMed: 33268889]
37. Olsen RHJ, DiBerto JF, English JG, Glaudin AM, Krumm BE, Slocum ST, Che T, Gavin AC, McCorvy JD, Roth BL, Strachan RT, TRUPATH, an open-source biosensor platform for interrogating the GPCR transducerome. Nature Chemical Biology 2020 16:8. 16, 841–849 (2020).
38. Gailly P, Najimi M, Hermans E, Evidence for the dual coupling of the rat neurotensin receptor with pertussis toxin-sensitive and insensitive G-proteins. FEBS Lett. 483, 109–113 (2000). [PubMed: 11042263]
39. Najimi M, Gailly P, Maloteaux JM, Hermans E, Distinct regions of C-terminus of the high affinity neurotensin receptor mediate the functional coupling with pertussis toxin sensitive and insensitive G-proteins. FEBS Lett. 512, 329–333 (2002). [PubMed: 11852105]
40. Okashah N, Wan Q, Ghosh S, Sandhu M, Inoue A, Vaidehi N, Lambert NA, Variable G protein determinants of GPCR coupling selectivity. Proc Natl Acad Sci U S A. 116, 12054–12059 (2019). [PubMed: 31142646]

41. van Eps N, Altenbach C, Caro LN, Latorraca NR, Hollingsworth SA, Dror RO, Ernst OP, Hubbell WL, Gi- and Gs-coupled GPCRs show different modes of G-protein binding. Proc Natl Acad Sci U S A. 115, 2383–2388 (2018). [PubMed: 29463720]
42. Slosky LM, Bai Y, Toth K, Ray C, Rochelle LK, Badea A, Chandrasekhar R, Pogorelov VM, Abraham DM, Atluri N, Peddibhotla S, Hedrick MP, Hershberger P, Maloney P, Yuan H, Li Z, Wetsel WC, Pinkerton AB, Barak LS, Caron MG, β-Arrestin-Biased Allosteric Modulator of NTSR1 Selectively Attenuates Addictive Behaviors. Cell. 181, 1364–1379.e14 (2020). [PubMed: 32470395]
43. Neer EJ, Pulsifer L, Wolf LG, The amino terminus of G protein α subunits is required for interaction with βγ. Journal of Biological Chemistry. 263, 8996–9000 (1988). [PubMed: 3132454]
44. Wall M, Posner B, Sprang S, Structural basis of activity and subunit recognition in G protein heterotrimers. Structure. 6, 1169–1183 (1998). [PubMed: 9753695]
45. a Wall M, Coleman DE, Lee E, a Iñiguez-Lluhi J, a Posner B, Gilman a G., Sprang SR, The structure of the G protein heterotrimer Gi alpha 1 beta 1 gamma 2. Cell. 83, 1047–1058 (1995). [PubMed: 8521505]
46. Bhattacharya S, Vaidehi N, Differences in Allosteric Communication Pipelines in the Inactive and Active States of a GPCR. Biophys J. 107, 422–434 (2014). [PubMed: 25028884]
47. Ma N, Nivedha AK, Vaidehi N, Allosteric communication regulates ligand-specific GPCR activity. FEBS J. 288, 2502–2512 (2021). [PubMed: 33738925]
48. Nivedha AK, Tautermann CS, Bhattacharya S, Lee S, Casarosa P, Kollak I, Kiechle T, Vaidehi N, Identifying functional hotspot residues for biased ligand design in G-protein-coupled receptors. Mol Pharmacol. 93, 288–296 (2018). [PubMed: 29367258]
49. Vaidehi N, Bhattacharya S, Allosteric Communication Pipelines in G-protein-coupled receptors. Curr Opin Pharmacol. 30, 76–83 (2016). [PubMed: 27497048]
50. Coleman DE, Berghuis AM, Lee E, Linder ME, Gilman AG, Sprang SR, Structures of active conformations of Gi alpha 1 and the mechanism of GTP hydrolysis. Science. 265, 1405–12 (1994). [PubMed: 8073283]
51. Goricanec D, Hagn F, NMR backbone and methyl resonance assignments of an inhibitory G-alpha subunit in complex with GDP. Biomolecular NMR Assignments 2018 13:1. 13, 131–137 (2018).
52. Koehl A, Hu H, Maeda S, Zhang Y, Qu Q, Paggi JM, Latorraca NR, Hilger D, Dawson R, Matile H, Schertler GFX, Granier S, Weis WI, Dror RO, Manglik A, Skiniotis G, Kobilka BK, Structure of the μ-opioid receptor–Gi protein complex. Nature 2018 558:7711. 558, 547–552 (2018).
53. Willard FS, Kimple AJ, Johnston CA, Siderovski DP, A direct fluorescence-based assay for RGS domain GTPase accelerating activity. Anal Biochem. 340, 341–351 (2005). [PubMed: 15840508]
54. McEwen DP, Gee KR, Kang HC, Neubig RR, Fluorescent BODIPY-GTP analogs: Real-time measurement of nucleotide binding to G proteins. Anal Biochem. 291, 109–117 (2001). [PubMed: 11262163]
55. Isom DG, Sridharan V, Baker R, Clement ST, Smalley DM, Dohlman HG, Protons as second messenger regulators of G protein signaling. Mol Cell. 51, 531–538 (2013). [PubMed: 23954348]
56. Niesen FH, Berglund H, Vedadi M, The use of differential scanning fluorimetry to detect ligand interactions that promote protein stability. Nat Protoc. 2, 2212–2221 (2007). [PubMed: 17853878]
57. Goricanec D, Stehle R, Egloff P, Grigoriu S, Plückthun A, Wagner G, Hagn F, Conformational dynamics of a G-protein α subunit is tightly regulated by nucleotide binding. Proc Natl Acad Sci U S A. 113, E3629–E3638 (2016). [PubMed: 27298341]
58. Mase Y, Yokogawa M, Osawa M, Shimada I, Backbone resonance assignments for G protein α(i3) subunit in the GDP-bound state. Biomol NMR Assign. 8, 237–241 (2014). [PubMed: 23771857]
59. Feng X, Arang N, Rigiracciolo DC, Lee JS, Yeerna H, Wang Z, Lubrano S, Kishore A, Pachter JA, König GM, Maggiolini M, Kostenis E, Schlaepfer DD, Tamayo P, Chen Q, Ruppin E, Gutkind JS, A Platform of Synthetic Lethal Gene Interaction Networks Reveals that the GNAQ Uveal Melanoma Oncogene Controls the Hippo Pathway through FAK. Cancer Cell. 35, 457–472.e5 (2019). [PubMed: 30773340]
60. Armbruster BN, Li X, Pausch MH, Herlitze S, Roth BL, Evolving the lock to fit the key to create a family of G protein-coupled receptors potently activated by an inert ligand. Proc Natl Acad Sci U S A. 104, 5163–5168 (2007). [PubMed: 17360345]

61. Gerdes J, Lemke H, Baisch H, Wacker HH, Schwab U, Stein H, Cell cycle analysis of a cell proliferation-associated human nuclear antigen defined by the monoclonal antibody Ki-67. The Journal of Immunology. 133, 1710–1715 (1984). [PubMed: 6206131]
62. a Landis C, Masters SB, Spada A, Pace a M., Bourne HR, Vallar L, GTPase inhibiting mutations activate the alpha chain of Gs and stimulate adenylyl cyclase in human pituitary tumours. Nature. 340, 692–696 (1989). [PubMed: 2549426]
63. Lyons J, Landis CA, Harsh G, Vallar L, Grünewald K, Feichtinger H, Duh QY, Clark OH, Kawasaki E, Bourne HR, Mccormick F, Two G protein oncogenes in human endocrine tumors. Science. 249, 655–658 (1990). [PubMed: 2116665]
64. Weinstein LS, Shenker A, Friedman E, Spiegel AM, Gejman P. v., Merino MJ, Activating mutations of the stimulatory g protein in the mcCune–albright syndrome. New England Journal of Medicine. 325, 1688–1695 (1991). [PubMed: 1944469]
65. Chua V, Lapadula D, Randolph C, Benovic JL, Wedegaertner PB, Aplin AE, Dysregulated GPCR Signaling and Therapeutic Options in Uveal Melanoma. Molecular Cancer Research. 15, 501–506 (2017). [PubMed: 28223438]
66. Kostenis E, Pfeil EM, Annala S, Heterotrimeric Gq proteins as therapeutic targets? Journal of Biological Chemistry. 295, 5206–5215 (2020). [PubMed: 32122969]
67. Smrcka A. v., Molecular targeting of Gα and Gβγ subunits: a potential approach for cancer therapeutics. Trends Pharmacol Sci. 34, 290 (2013). [PubMed: 23557963]
68. Traut TW, Physiological concentrations of purines and pyrimidines. Mol Cell Biochem. 140, 1–22 (1994). [PubMed: 7877593]
69. Nishimura A, Kitano K, Takasaki J, Taniguchi M, Mizuno N, Tago K, Hakoshima T, Itoh H, Structural basis for the specific inhibition of heterotrimeric G q protein by a small molecule. Proc Natl Acad Sci U S A. 107, 13666–13671 (2010). [PubMed: 20639466]
70. Takasaki J, Saito T, Taniguchi M, Kawasaki T, Moritani Y, Hayashi K, Kobori M, A Novel Gαq/11-selective Inhibitor *. Journal of Biological Chemistry. 279, 47438–47445 (2004). [PubMed: 15339913]
71. Schrage R, Schmitz AL, Gaffal E, Annala S, Kehraus S, Wenzel D, Büllesbach KM, Bald T, Inoue A, Shinjo Y, Galandrin S, Shridhar N, Hesse M, Grundmann M, Merten N, Charpentier TH, Martz M, Butcher AJ, Slodczyk T, Armando S, Effern M, Namkung Y, Jenkins L, Horn V, Stößel A, Dargatz H, Tietze D, Imhof D, Gales C, Drewke C, Müller CE, Hölzel M, Milligan G, Tobin AB, Gomeza J, Dohlman HG, Sondek J, Harden TK, Bouvier M, Laporte SA, Aoki J, Fleischmann BK, Mohr K, König GM, Tüting T, Kostenis E, The experimental power of FR900359 to study Gq-regulated biological processes. Nature Communications 2015 6:1. 6, 1–17 (2015).
72. Xiong XF, Zhang H, Underwood CR, Harpsøe K, Gardella TJ, Wöldike MF, Mannstadt M, Gloriam DE, Bräuner-Osborne H, Strømgaard K, Total synthesis and structure-activity relationship studies of a series of selective G protein inhibitors. Nat Chem. 8, 1035–1041 (2016). [PubMed: 27768111]
73. Onken MD, Makepeace CM, Kaltenbronn KM, Kanai SM, Todd TD, Wang S, Broekelmann TJ, Rao PK, Cooper JA, Blumer KJ, Targeting nucleotide exchange to inhibit constitutively active G protein a subunits in cancer cells. Sci Signal. 11 (2018) (available at https://www.science.org).
74. Annala S, Feng X, Shridhar N, Eryilmaz F, Patt J, Yang J, Pfeil EM, Daniel Cervantes-Villagrana R, Inoue A, Häberlein F, Slodczyk T, Reher R, Kehraus S, Monteleone S, Schrage R, Heycke N, Rick U, Engel S, Pfeifer A, Kolb P, König G, Bünemann M, Tüting T, Vázquez-Prado J, Gutkind JS, Gaffal E, Kostenis E, Direct targeting of Gα q and Gα 11 oncoproteins in cancer cells. Sci. Signal 12, 5948 (2019).
75. Maly J, Crowhurst KA, Expression, purification and preliminary NMR characterization of isotopically labeled wild-type human heterotrimeric G protein αi1. Protein Expr Purif. 84, 255–264 (2012). [PubMed: 22713620]
76. Huynh K, Partch CL, Curr Protoc Protein Sci, in press, doi:10.1002/0471140864.ps2809s79.
77. Micsonai A, Wien F, Bulyáki É, Kun J, Moussong É, Lee YH, Goto Y, Réfrégiers M, Kardos J, BeStSel: A web server for accurate protein secondary structure prediction and fold recognition from the circular dichroism spectra. Nucleic Acids Res. 46, W315–W322 (2018). [PubMed: 29893907]

78. Waterhouse A, Bertoni M, Bienert S, Studer G, Tauriello G, Gumienny R, Heer FT, de Beer TAP, Rempfer C, Bordoli L, Lepore R, Schwede T, SWISS-MODEL: homology modelling of protein structures and complexes. Nucleic Acids Res. 46, W296–W303 (2018). [PubMed: 29788355]

79. Jo S, Kim T, Iyer VG, Im W, CHARMM-GUI: A web-based graphical user interface for CHARMM. J Comput Chem. 29, 1859–1865 (2008). [PubMed: 18351591]

80. Huang J, Rauscher S, Nawrocki G, Ran T, Feig M, de Groot BL, Grubmüller H, MacKerell AD, CHARMM36m: An improved force field for folded and intrinsically disordered proteins. Nat Methods. 14, 71–73 (2016). [PubMed: 27819658]

81. Berendsen HJC, van der Spoel D, van Drunen R, GROMACS: A message-passing parallel molecular dynamics implementation. Comput Phys Commun. 91, 43–56 (1995).

82. Darden T, York D, Pedersen L, Particle mesh Ewald: An N·log(N) method for Ewald sums in large systems. J Chem Phys. 98, 10089–10092 (1993).

83. Martyna GJ, Klein ML, Tuckerman M, Nosé-Hoover chains: The canonical ensemble via continuous dynamics. J Chem Phys. 97, 2635–2643 (1992).

84. Parrinello M, Rahman A, Polymorphic transitions in single crystals: A new molecular dynamics method. J Appl Phys. 52, 7182–7190 (1981).

85. Pedregosa F, Michel V, Grisel O, Blondel M, Prettenhofer P, Weiss R, Vanderplas J, Cournapeau D, Pedregosa F, Varoquaux G, Gramfort A, Thirion B, Grisel O, Dubourg V, Passos A, Brucher M, Édouard Duchesnay M, Scikit-learn: Machine Learning in Python. Journal of Machine Learning Research. 12, 2825–2830 (2011).

86. Vaqué JP, Dorsam RT, Feng X, Iglesias-Bartolome R, Forsthoefel DJ, Chen Q, Debant A, Seeger MA, Ksander BR, Teramoto H, Gutkind JS, A genome-wide RNAi screen reveals a Trio-regulated Rho GTPase circuitry transducing mitogenic signals initiated by G protein-coupled receptors. Mol Cell. 49, 94–108 (2013). [PubMed: 23177739]

87. Cappell SD, Baker R, Skowyra D, Dohlman HG, Systematic Analysis of Essential Genes Reveals New Regulators of G protein Signaling. Mol Cell. 38, 746 (2010). [PubMed: 20542006]

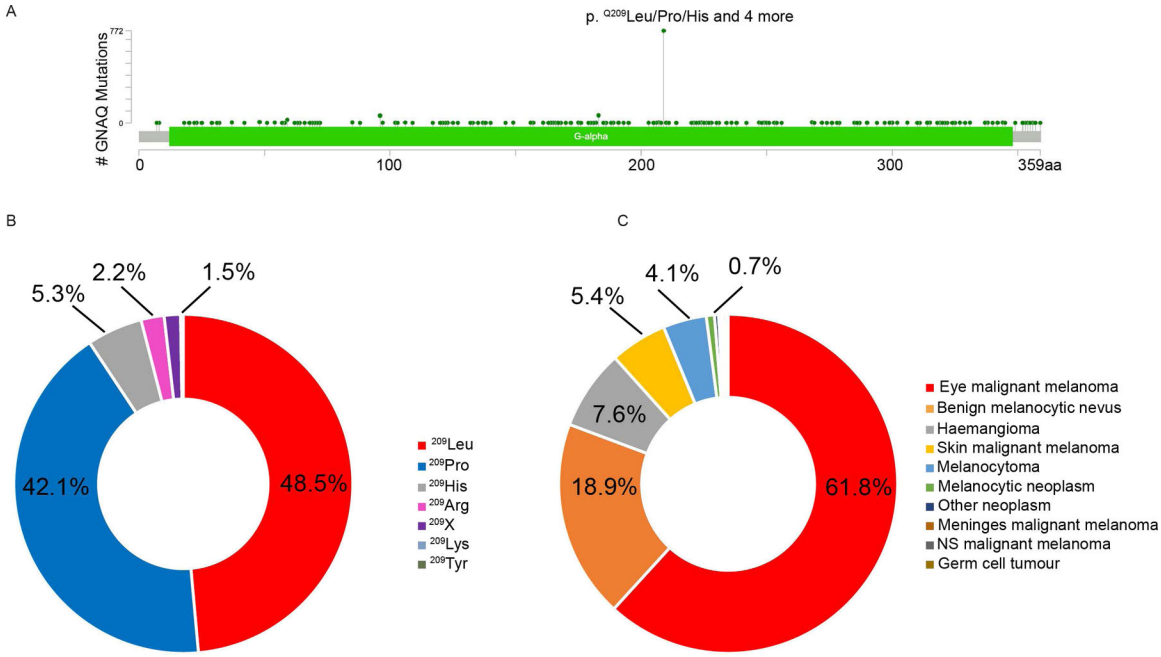

Fig. 1. Prevalence and distribution of catalytic glutamine mutations in cancer.

(**A**) Graphical view of all of the mutations found in *GNAQ* from patient samples curated by COSMIC (v94). (**B**) Pie chart showing the distribution of observed substitutions in $G\alpha_q$ from patient samples. (**C**) Pie chart showing the tissue distribution of catalytic glutamine mutations.

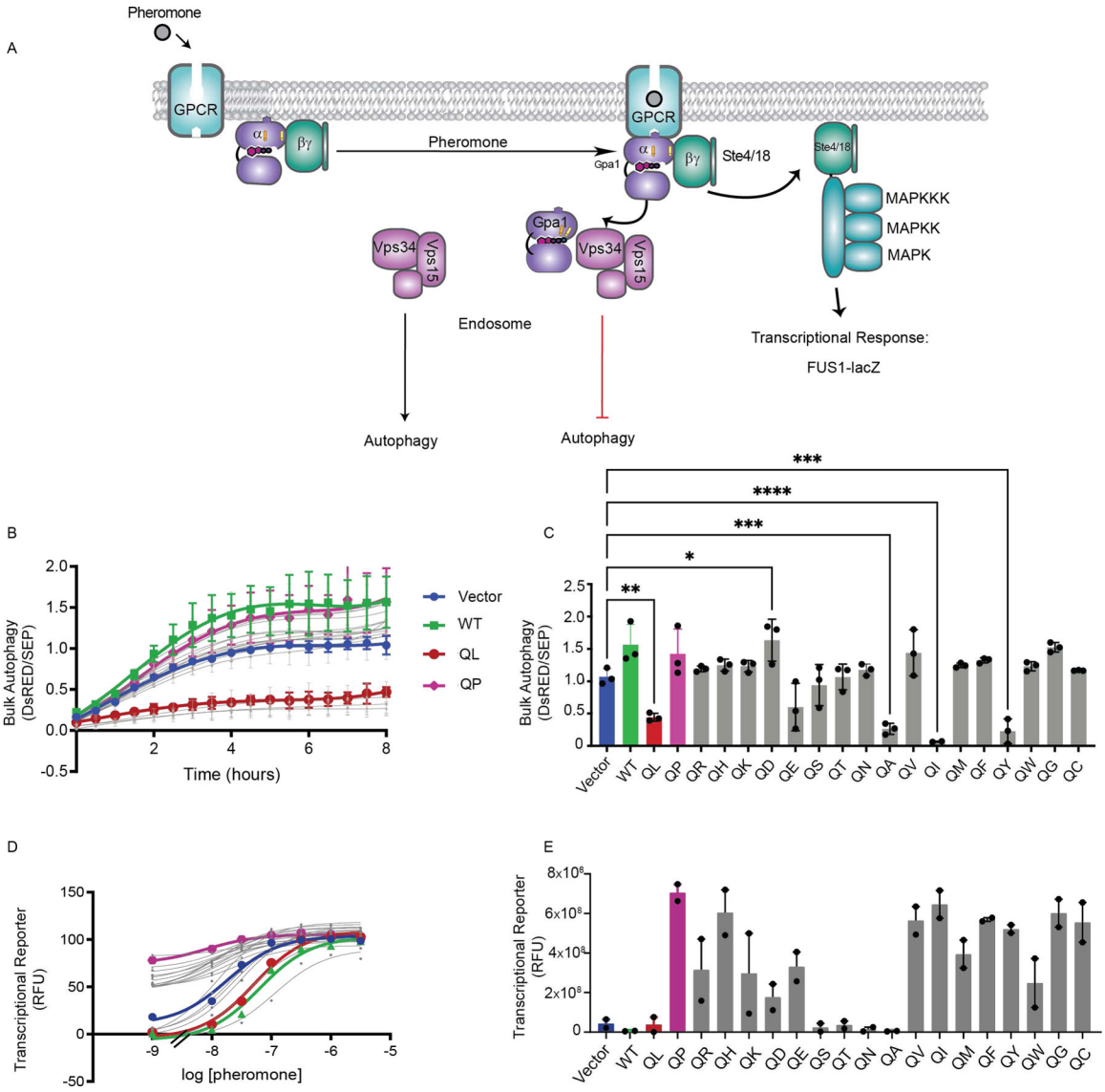

Fig. 2. Catalytic glutamine mutations confer distinct Gα- and Gβγ-mediated signaling outputs.

(**A**) The yeast mating pathway is activated by the binding of pheromone to the GPCR (Ste2). Ste2 catalyzes the exchange of GDP for GTP and dissociation of Gα (Gpa1) from Gβγ (Ste4/Ste18). Ste4/Ste18 activates a MAPK kinase kinase (Ste11), a MAPK kinase (Ste7), and the terminal MAPK (Fus3). Fus3 promotes induction of mating genes. Gpa1 binds to the sole phosphatidylinositol 3-kinase in yeast, Vps34, and the Gβ-like regulatory subunit, Vps15, which promote autophagy under nitrogen-deficient conditions. (**B**) The autophagy biosensor Rosella was used to measure Gpa1-dependent cytoplasm-to-vacuole targeting in BY4741 *bar1*Δ (wild-type) cells. Time-course of vacuole targeting initiated by nitrogen depletion in wild-type cells with plasmids expressing Gpa1 wild-type (WT), the indicated Gpa1 mutants, or vector with no insert (pRS316). Fluorescence was measured every 30 min for 8 hours.(**C**) Rosella assay values measured at 8 hours. (**D**) The *FUS1*-lacZ transcriptional reporter was used to measure Ste4/18-dependent transcription in wild-type cells transformed with Gpa1 WT, Gpa1 mutants, or vector with no insert (pRS316). Cells were treated with 0

to 3 μM α-factor pheromone, and fluorescence was measured after 90 min. Data represent the percentage of maximum transcriptional activity in cells relative to that in cells with empty vector. (**E**) Transcriptional reporter activity when no α-factor was added. Symbols in (B) and bars in (C) are means ± SD from three independent experiments with two measurements each. Pair-wise comparisons with vector are $*P < 0.05$, $**P < 0.01$, $***P < 0.001$, and $****P < 0.0001$ by one-way ANOVA. Symbols in (D) and bars in (E) are the means of two independent experiments with two measurements each.

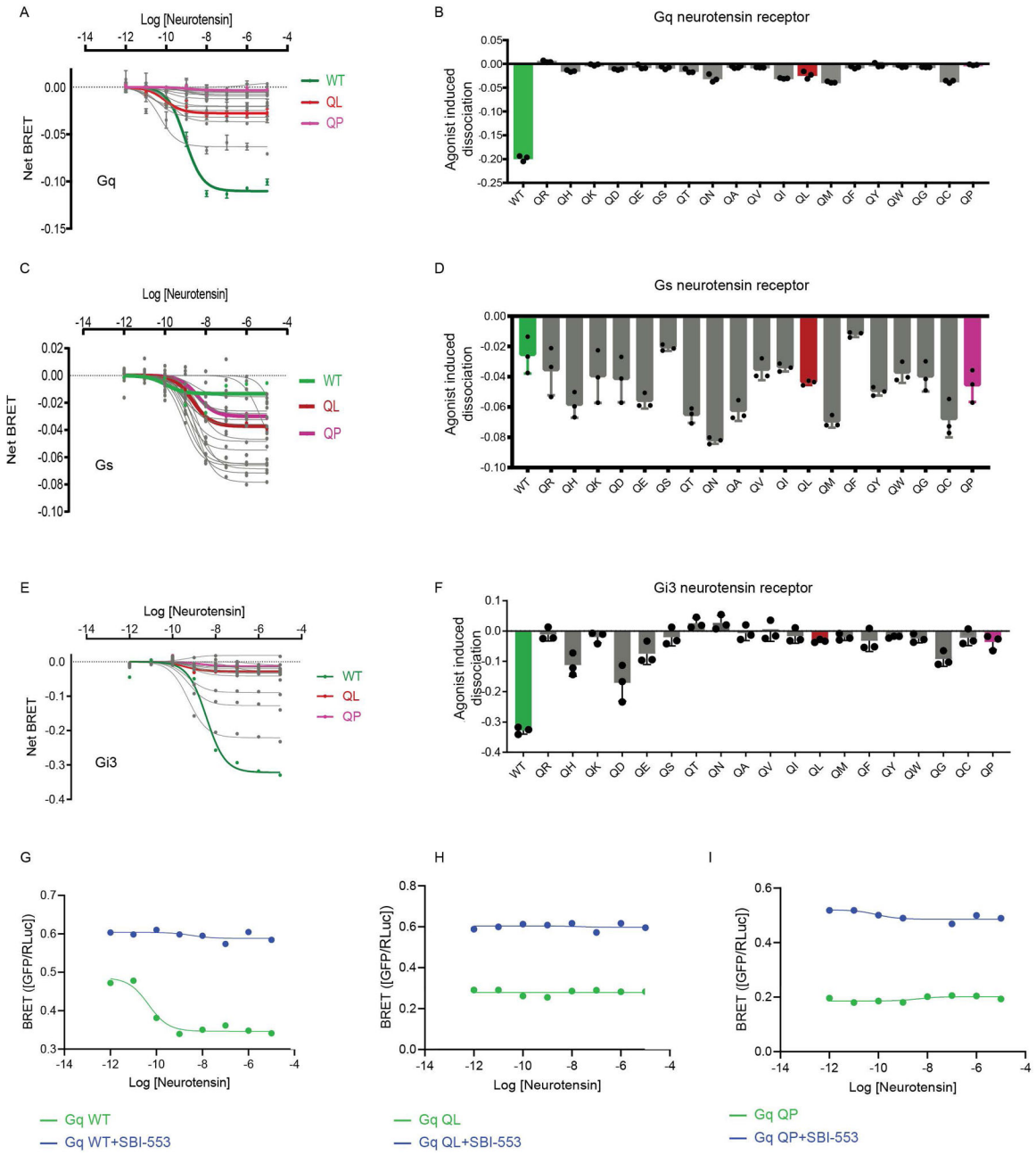

Fig. 3. Catalytic glutamine mutations confer substitution- and subtype-specific activation by GPCRs.

(**A** to **I**) G protein subunit dissociation was measured with TRUPATH biosensors consisting of Gα-RLuc8 (donor), $G\beta_3$, and $G\gamma_9$-GFP2 (acceptor), which were activated by stimulation of the neurotensin receptor 1 (NTR1) in HEK293T cells. Cells were treated with the indicated concentrations of neurotensin, and the ratio of GFP2 to RLuc8 was measured. (A) BRET for wild-type (WT, green), QL (red), QP (magenta), and 17 other (gray) mutant forms of $G\alpha_q$. (B) Net BRET at the highest agonist concentration, in bar-graph form. (C) $G\alpha_s$ BRET. (D) Net BRET for $G\alpha_s$. (E) $G\alpha_{i3}$ BRET. (F) Net BRET $G\alpha_{i3}$. (G) BRET for WT $G\alpha_q$ without (green) or with (blue) SBI-553 allosteric ligand treatment. (H) BRET for

$G\alpha_q$ QL without (green) or with (blue) SBI-553 treatment. (I) BRET for $G\alpha_q$ QP without (green) or with (blue) SBI-553 treatment. Data in (A), (C), (E) and (G to I) are means (symbols) from two measurements and are representative of three independent experiments. Data in (B), (D), and (F) are means ± SD from three independent experiments (symbols) with two measurements each. In (B), all pair-wise comparisons with WT were $P < 0.0001$ by one-way ANOVA. In (D), pair-wise comparisons with WT were $*P < 0.05$, $**P < 0.01$, $***P < 0.001$, and $****P < 0.0001$ by one-way ANOVA.

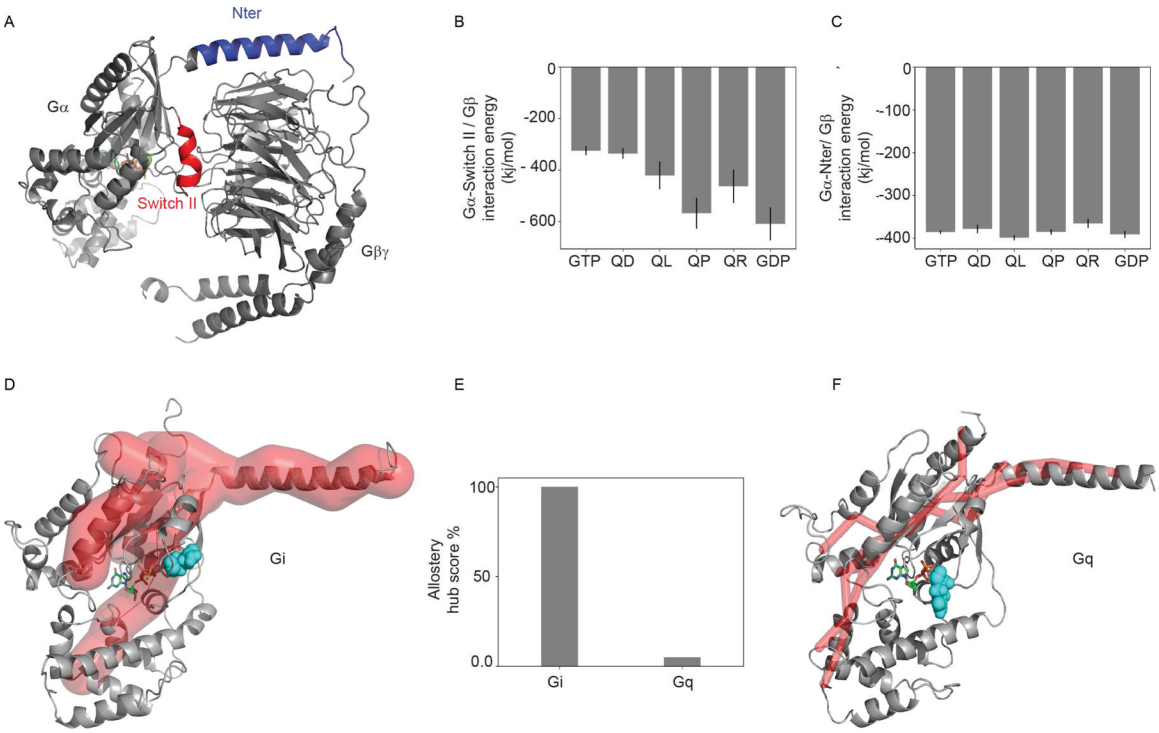

Fig. 4. Catalytic glutamine mutations confer substitution- and subtype-specific interaction energies.

(**A**) Structure of the $G\alpha_{i1}\beta\gamma$ trimer (PDB ID: 1GP2). The red region is Switch II, the blue region is the N terminus of the Gα unit. (**B**) Interaction energies between $G\alpha_i$ Switch II and Gβ, averaged across the three MD simulation runs, for WT-GTP/GDP and the indicated mutants. The error bars indicate the SD across the three simulations. (**C**) Interaction energies between the $G\alpha_i$ N terminus and Gβ, averaged across the MD simulation trajectories, for WT-GTP/GDP and the indicated mutants. (**D**) Allosteric communication pipeline (tube in red) starting from the Gαβ interface residues and passing through the nucleotide-binding site to the C-terminal residues in $G\alpha_i$. The radius of the red tube is proportional to allosteric communication strength. The nucleotide is shown as sticks and Gln^{204} is shown as a cyan sphere. (**E**) Normalized allosteric hub score comparison between $G\alpha_i$ and $G\alpha_q$. A greater score means stronger contribution to the allosteric communication. (**F**) Allosteric communication pipeline (tube in red) starting from the Gαβ interface and passing through the nucleotide-binding site to the C terminus in $G\alpha_q$. The radius of the red tube is proportional to allosteric communication strength. The nucleotide is shown as sticks and Gln^{209} is shown as a cyan sphere. Data in (B) and (C) are means ± SD from three independent simulations.

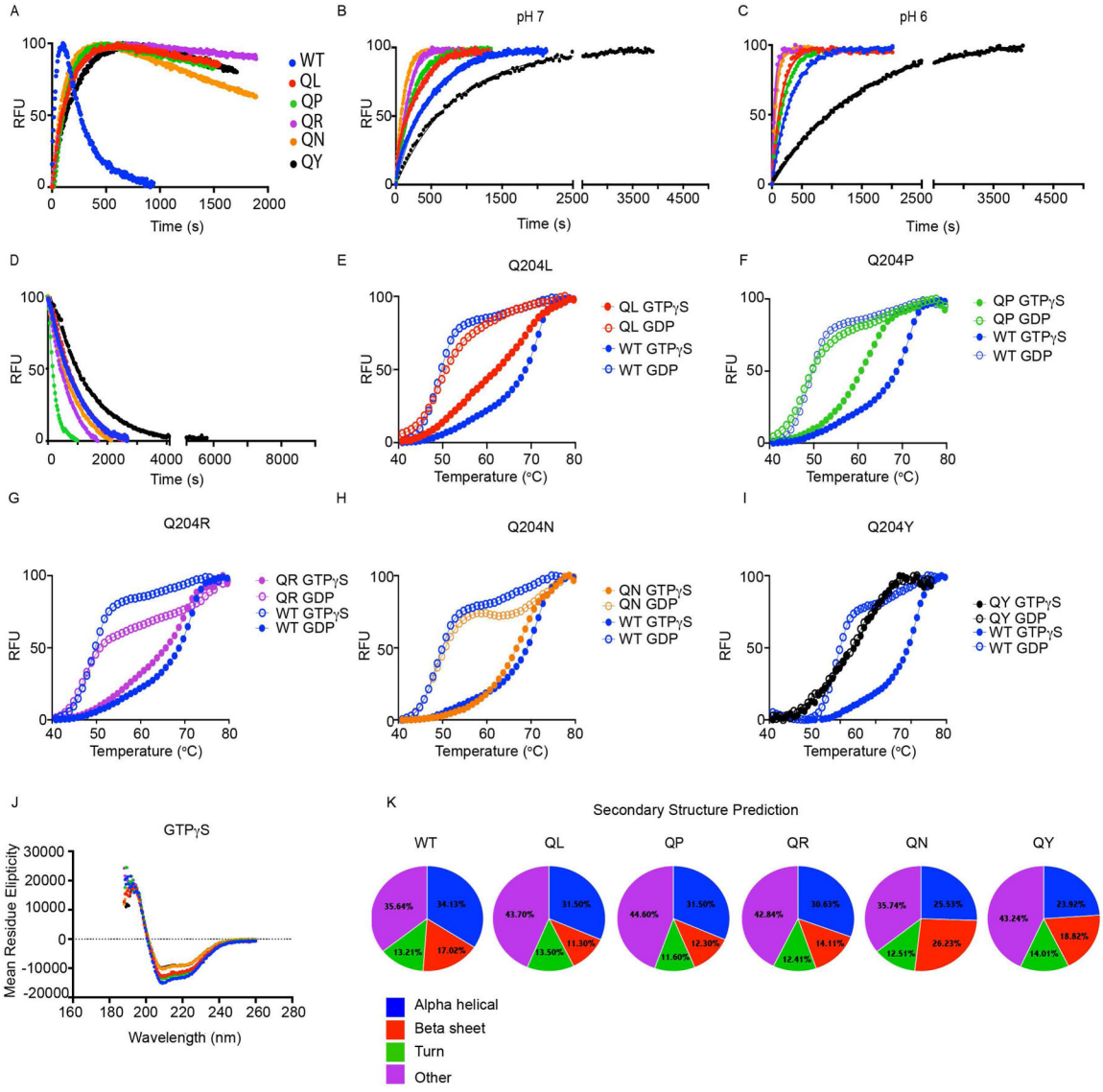

Fig. 5. Biophysical characterization of glutamine mutants.

(**A**) Gα_{i1}-GDP was combined with BODIPY-GTP, and binding and hydrolysis were assessed by measuring the increase and decrease in fluorescence, respectively. RFU, relative fluorescence units. (**B**) Gα_{i1}-GDP was combined with a nonhydrolyzable GTP analog, BODIPY-GTPγS at pH 7. The intrinsic rate of exchange was determined by measuring the increase in fluorescence. (**C**) Gα_{i1}-GDP was combined with BODIPY-GTPγS at pH 6. (**D**) Gα_{i1} bound to BODIPY-GTPγS was combined with excess GTPγS. The rate of dissociation was measured as the decrease in fluorescence. (**E** to **I**) Thermostability of Gα_{i1} in GDP-and GTPγS-bound states, as determined by SYPRO fluorescence labeling of buried hydrophobic regions. (**J**) Circular dichroism (CD) spectrum analysis for Gα_{i1} WT and the indicated mutants, in the GTPγS-bound state. Spectral scans ranged from 185 to 260 nm at 30°C (shown), and 70 and 90°C (fig. S3, F and G). (**K**) Secondary structure predictions based on CD measurements. Data in (A to D) are representative of three independent experiments, and are fit to one phase exponential decay curves. In (B) and (C), pair-wise comparisons

of WT and mutants are $^{**}P < 0.01$ and $^{****}P < 0.0001$ respectively, by one-way ANOVA. Data in (E to J) are representative of two independent experiments, and are fit to Boltzmann sigmoidal curves.

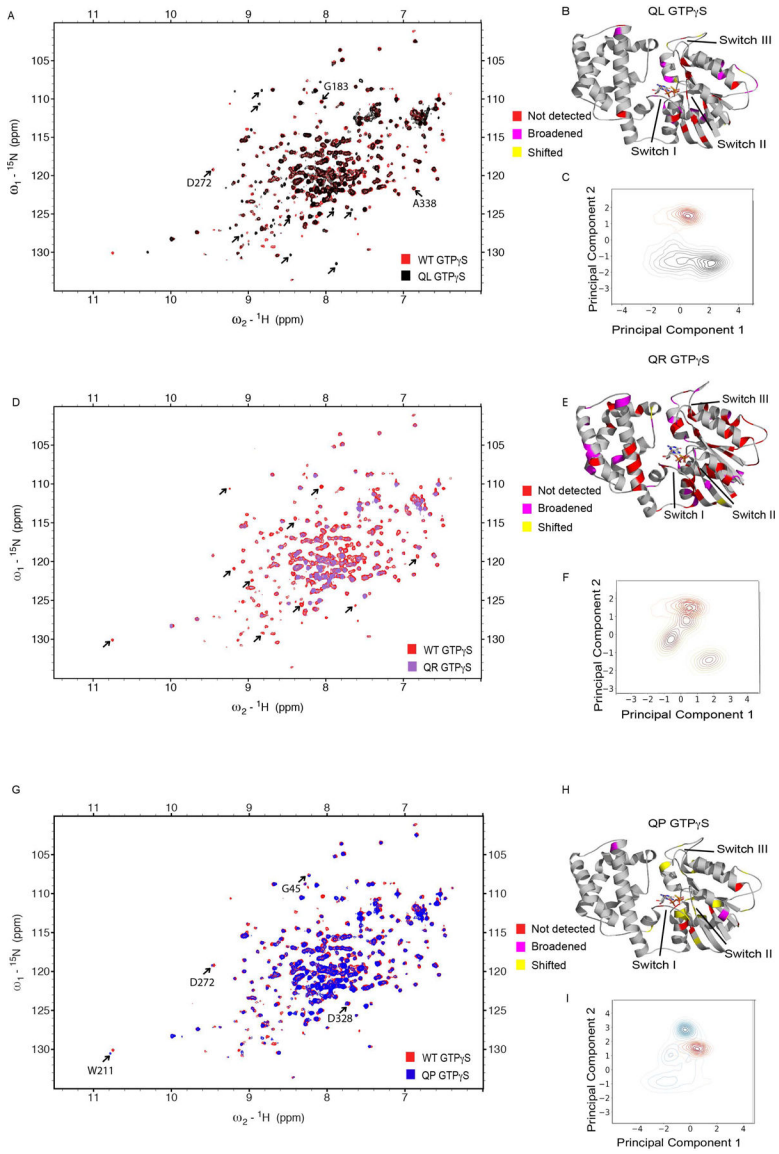

Fig. 6. NMR HSQC spectral overlay of GTPγS-bound wild-type $G\alpha_{i1}$ with the QL, QR, and QP mutants.

(A) 2D [^{15}N, ^{1}H] HSQC NMR spectra were acquired on a Bruker Avance 850 at 25°C for 100 to 200 μM ^{15}N-enriched $G\alpha_{i1}$. Decreases in peak intensity indicate line broadening. Shifts in peak position relative to the assigned WT were considered as chemical shifts. Peaks missing in the mutant spectrum relative to the WT were considered as undetected peaks. Spectral overlay of WT (red) and QL (black) in the GTPγS-bound state. The WT had approximately 310 peaks and the QL mutant had 372 peaks in total. Spectral overlay shows extensive peak broadening relative to chemical shift changes for QL and a subset of 60 peaks not evident in the WT. Labeled arrows indicate examples of broadened residues in the QL spectrum. Unlabeled arrows indicate an example of undetected peaks in the QL spectrum. (**B**) Structural rendering of the $G\alpha_{i1}$ structure with PyMOL (PDB: 1GIL), highlighting undetected peaks (red), shifted peaks (CSP, chemical shift perturbation > 1.4; yellow), and broadened peaks (magenta) in QL. (**C**) Projecting MD simulation trajectory snapshots of

WT (red) and QL (black) onto PC1 and PC2. The contour line is related to population density with a darker color indicating greater density. (**D**) Spectral overlay of WT $G\alpha_{i1}$ (red) and the QR mutant (purple) in the GTPγS-bound state. The QR has 100 fewer peaks than those seen for the WT. Spectral overlay shows extensive resonance-broadening in both the RAS-like and helical domain. Arrows indicate undetected peaks in the QR spectrum. (**E**) Structural rendering of the $G\alpha_{i1}$ structure with PyMOL (PDB:1GIL) highlighting undetected peaks (red), shifted peaks (yellow), and broadened peaks (magenta) in QR. (**F**) Projecting MD simulation trajectory snapshots of WT (red) and QR (magenta) onto PC1 and PC2. The contour line is related to the population density, with a darker color indicating greater density. (**G**) Spectral overlay of WT $G\alpha_{i1}$ (red) and the QP mutant (blue) in the GTPγS-bound state. QP has 312 peaks in total. Spectral overlay shows chemical shift changes in the RAS-like domain relative to that of the WT. Arrows indicate examples of shifted peaks in the spectrum of QP in putative nucleotide-binding regions (G-boxes). (**H**) Structural rendering of the $G\alpha_{i1}$ structure with PyMOL (PDB: 1GIL) highlighting undetected peaks (red), shifted peaks (yellow), and broadened peaks (magenta) in QP. (**I**) Projection of MD simulation trajectory snapshots of WT (red) and QP (blue) onto PC1 and PC2. The contour line is related to the population density, with a darker color indicating greater density. Data in (A), (D), and (G) are representative of two independent experiments.

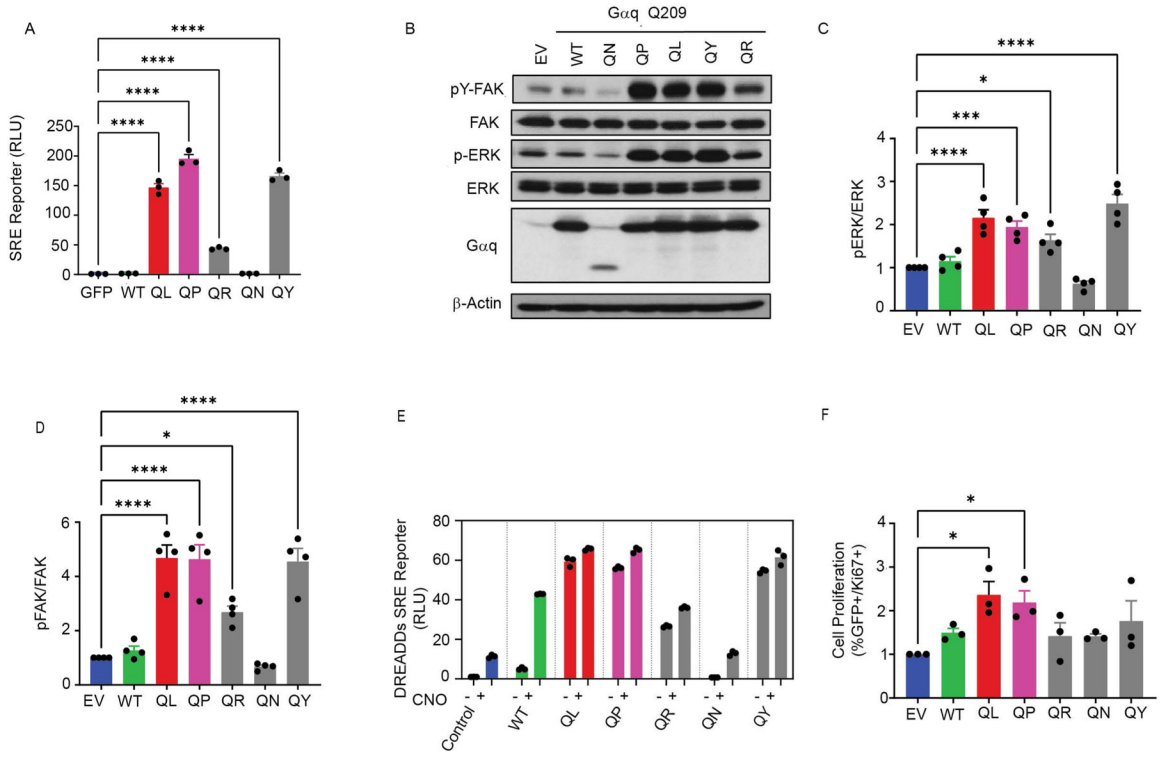

Fig. 7. Catalytic glutamine mutations confer distinct Gα-mediated signaling outputs in mammalian cells.

(**A**) SRE-luciferase reporter activity in HEK293 cells co-transfected with a plasmid expressing SRE-luc reporter in combination with control vector (GFP), or plasmids encoding $G\alpha_q$ WT or the indicated glutamine mutants. (**B**) Representative Western blotting analysis of FAK and ERK phosphorylation in HEK293 cells transfected with empty vector (EV) or plasmids encoding $G\alpha_q$ WT or the indicated glutamine mutants. (**C**) Quantification of the amount of phosphorylated ERK (pERK) relative to that of total ERK from the experiments shown in (B). (**D**) Quantification of the amount of phosphorylated FAK (pFAK) relative to that of total FAK from the experiments shown in (B). (**E**) SRE-luciferase reporter activity in HEK293 cells cotransfected with the SRE-luc reporter and $G\alpha_q$-DREADD in combination with empty vector control (EV) or plasmids encoding $G\alpha_q$ WT or the indicated glutamine mutants. Reporter activity was measured under basal conditions and in response to 1 μM CNO for 6 hours. (**F**) Cell proliferation in NIH3T3 cells co-transfected with GFP and empty vector control (EV) or plasmids encoding $G\alpha_q$ WT or the indicated glutamine mutants. Measurement of the percentage of $GFP^+/Ki67^+$ cells was used to assess the proportion of transfected proliferative cells. Data in (A) and (C to F) are means ± SEM from three independent experiments (symbols) with three measurements each. $*P < 0.05$, $***P < 0.001$, and $****P < 0.0001$ by one-way ANOVA. Data in (B) are representative of three independent experiments.